Journal of Solid State Electrochemistry (2020) 24:473–497
https://doi.org/10.1007/s10008-019-04467-3

REVIEW PAPER

Review on synthesis methods to obtain $LiMn_2O_4$-based cathode materials for Li-ion batteries

Alexandru-Horatiu Marincaş[1] · Firuța Goga[1] · Sorin-Aurel Dorneanu[1,2] · Petru Ilea[1,2]

Received: 25 July 2019 / Revised: 6 December 2019 / Accepted: 6 December 2019 / Published online: 7 January 2020

Abstract

Lithium manganese spinel ($LiMn_2O_4$) is considered a promising cathode material for lithium-ion batteries (LIBs). Its structure, morphology, and electrochemical performances are strongly connected to the precursors, synthesis route, and heat treatment; hence, by optimizing the synthesis procedure, improved materials can be obtained. Recently investigated routes focus on the synthesis of enhanced $LiMn_2O_4$ spinel, with uniform morphology, high crystallinity, which can deliver large discharge capacity at high rates for a longer period of time. Also, the synthesis procedure must be easily applicable on industrial scale, not just for pilot and laboratory investigations. In the current study, main synthesis procedures (solid-state reactions, sol-gel, hydrothermal reactions, combustion method plus several newly employed methods) used for obtaining lithium manganese oxide, along with its electrochemical effectiveness, are described. Among the considered synthesis methods, some of the best electrochemical performances are recorded for lithium manganese oxide obtained by sol-gel process and hydrothermal method. Even though solid-state reaction method is a simple and has few stages, particle crystallinity and size are more difficult to control, while sol-gel and hydrothermal method provides more evenly sized particles. Also, the latter two syntheses do not need very high calcination temperatures like in the samples obtained by solid-state reactions method. Lithium manganese spinel with uniform spherical and octahedral particles delivered the highest initial discharge capacities and has the ability to retain most of the capacity during the charge–discharge cycles.

Keywords Lithium manganese oxide · Spinel · Cathode material · Li-ion batteries · Synthesis methods

Introduction

Late developments in the field of new portable devices (laptops, smartphones, and digital cameras) and new electrical powered vehicles (hybrid electric cars, electric bicycles, electric scooter, and skateboards) demanded suitable power sources to meet their energy requirements. Thus, it was found out that Li-ion batteries (LIBs) provide the desired energy amount for the new devices and vehicles [1, 2]. Compared to conventional second-type batteries (lead-acid battery, Ni-MH or Ni-Cd batteries), LIBs provide superior energy density, longer life cycles, and higher operational voltage (in the range of 4 V) [3–5]. The functioning principle of Li-ion batteries is based on the intercalation of lithium ion from cathode material into graphitic anodic matrix during the cell's charging, while the electrons pass to anode matrix for tying up the Li^+. When the cell's discharge takes place, an opposite process occurs; Li ions pass the electrolyte solution, back to cathode material, while electrons are released into cell's external circuit [6, 7]. In 1980, J. B. Goodenough proposed the first suitable intercalation cathode material for a Li-ion battery and different material classes were studied since then: layered (lithium cobalt oxide, $LiCoO_2$, and lithium nickel oxide, $LiNiO_2$), spinel (lithium manganese oxide, $LiMnO_2$), and olivine (lithium iron phosphate, $LiFePO_4$) compounds, respectively [8–10].

Electronic supplementary material The online version of this article (https://doi.org/10.1007/s10008-019-04467-3) contains supplementary material, which is available to authorized users.

✉ Sorin-Aurel Dorneanu
dorneanu@chem.ubbcluj.ro

✉ Petru Ilea
pilea@chem.ubbcluj.ro

[1] Faculty of Chemistry and Chemical Engineering, Babeș Bolyai University, 11 Arany Janos Street, Cluj-Napoca, Romania

[2] Interdisciplinary Research Institute on Bio-Nano-Sciences, Babeș Bolyai University, 46 Treboniu Laurean Street, Cluj-Napoca, Romania

Cathode materials for Li-ion batteries

$LiCoO_2$ (LCO) is the most commercialized cathode material since the launching of Sony's Li-ion battery, back in 1991 [11]. Regarding the theoretical capacity of the abovementioned oxidic materials, $LiCoO_2$ and $LiNiO_2$ possess the highest theoretical capacity, 274 mAh g^{-1} and 275 mAh g^{-1}, respectively [12, 13]. The practical capacity provided by lithium cobalt oxide is half of its theoretical capacity, due to the impossibility to cycle more than 50% of Li ions without affecting the structure [5, 14]. Other drawbacks related to this cathode material are environmental toxicity cause by cobalt's presence and limited availability of raw materials which leads to high manufacture costs [15].

Although $LiNiO_2$ (LNO) was taken in consideration as an alternative for $LiCoO_2$ because of its high theoretical capacity (~275 mAh g^{-1}), plenty raw materials, its electrochemical performance is hindered by structure's instability, blocked lithium diffusion paths by Ni^{3+}, and difficult synthesis routes for obtaining compounds with good stoichiometry [16, 17]. Thus, the availability of Li-ion batteries with $LiNiO_2$ cathode is non-existent.

Having a theoretical capacity of 170 mAh g^{-1}, good thermal stability, and sufficient raw materials, $LiFePO_4$ (LFP) is considered a suitable cathode material for nowadays Li-ion batteries for portable devices and hybrid electric vehicles (hEV). Unfortunately, the pristine $LiFePO_4$ suffers from slow kinetics due to electronic and ionic conductivity [18, 19].

$LiMn_2O_4$ (LMO) is regarded as a capable cathode material for Li-ion batteries designed for electric vehicles, despite the fact that it can deliver a theoretical capacity of only 148 mAh g^{-1} [20]. In comparison to other cathode materials, LMO's advantages are related to low production cost, environmental friendliness, easy synthesis methods, and high rate capability [11, 21]. The main drawbacks of LMO are linked to relatively low practical achievable capacity (up to 135 mAh g^{-1} for the pristine sample [17, 22], but in certain synthesis condition, a capacity of 146 mAh g^{-1} can be achieved [23]) and capacity fading during long cycling tests because of:

(1) Dissolution of Mn^{2+} ions in the organic electrolyte during cycling, through the disproportionate reaction of.

$$2Mn^{3+} \rightarrow Mn^{4+} + Mm^{2+}$$ [1, 24–26]

(2) Structural Jahn–Teller distortion in the discharge state [26–28];
(3) The appearance of oxygen defects (during cycling at high potential values or after the spinel's synthesis at high temperatures) [26, 29, 30].

The current research provides an overview of synthesis methods used in LMO's fabrication and the electrochemical performances of LMO-based cathodes, over the last 11 years. An intensive literature review has been made, based on the information from Thomson Reuters's Web of Science (accessed on May 28, 2019). The graph from Fig. 1 was realized taken in consideration the publications where pristine, doped, and surface-coated LMO [11, 26, 31–35] were synthesized or where commercial $LiMn_2O_4$ was successfully used as cathode material. Also, other studies related to lithium ion batteries with LMO cathode and new synthesized anode material [36, 37] or numerical models of Li-ion batteries with lithium manganese oxide were studied [38, 39]. In addition, articles where LMO was part of blended cathode materials [40–42] and precursor for the synthesis of more complex oxides [43] were taken in consideration. The graph from Fig. 1 depicts a relative constant interest in developing improved intercalation compounds based on lithium manganese oxide in the last years.

While lithium cobalt oxide and lithium iron phosphate exhibit a layered structured and an olivine type structure, respectively, lithium manganese oxide presents a spinel crystallographic structure. Lithium manganese oxide's structure [44] belongs to Fd3m space group [45–47]. In a typical spinel structure with general formula $A[B_2]X_4$ (in this particular case, A corresponds to Li, B to manganese and X to oxygen), the lithium ions are located in 8a tetrahedral sites, manganese occupies 16d octahedral sites, while oxygen ions are place in 32e sites, resulting in a close-cubic package (*ccp*) array [48, 49] (Fig. 2). A diamond-shaped framework is formed by the $[MnO_6]^{2-}$ octahedral, which provides a 3D diffusion path for lithium ions, during the material's cycling [45, 46]. In comparison with LMO spinel, the layered intercalation compounds $LiCoO_2$ and $LiNiO_2$ furnish a 2D diffusion path, while olivine $LiFePO_4$ provides 1D lithium diffusion path [19, 50, 51]. Recently, $LiMn_2O_4$ spinel with 1D hollow structure was synthesized by Yang et al. [52] by single-spinneret electrospinning. The main advantages of this 1D structure consist in providing a high surface area, low risk of unit cell changing during the lithium ion intercalation/deintercalation processes, and more diffusion paths for Li^+ [52, 53].

Heat treatment is very important for obtaining the spinel structure through any synthesis method, because spinel structure demands higher calcination temperature and longer heat treatment duration than layered compounds ($LiMnO_2$). This aspect is related to the larger space between tetrahedral $[MnO_6]$ inside the layered $LiMnO_2$, which can easily accommodate hydrated cations, while in the spinel structure, the paths inside the 3D framework are narrower [55].

Lithium manganese oxide's stoichiometry ($Li_xMn_2O_4$) must be carefully controlled. $Li_xMn_2O_4$ exhibits a cubic structure, when $0 < x < 1$, and when a larger amount of lithium ions are inserted, a structure change with increased volume of the unit cell occurs, also known as Jahn–Teller distortion. Tetragonal $Li_{1+x}Mn_2O_4$ performs badly, showing a lower

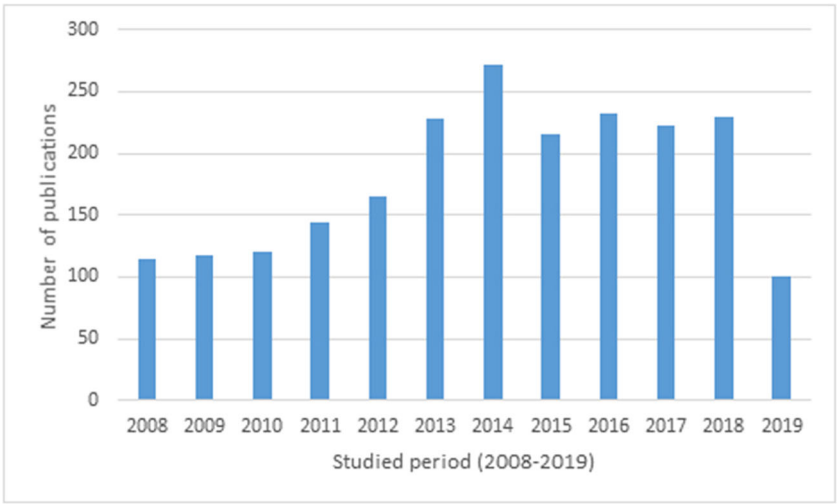

Fig. 1 Significant LMO articles published in the last years (2008–2019) (first 4 months)

discharge plateau, in the range of 3 V, while cubic spinel presents a two-stage discharge plateau at a higher potential of 4.1 and 4 V, respectively [56, 57].

Electrochemical behavior of $LiMn_2O_4$ cathode material

In a battery which employs LMO spinel as cathode material, the lithium intercalation/deintercalation processes take place in two stages during battery charging and discharging, not as in one stage as for other cathode materials (LCO, LNO, LFP) [58–60]. Throughout battery's charging, half of lithium ions, between which Li-Li interactions exist, are extracted from its 8a tetrahedral sites, followed by the deintercalation of the other half of Li-Li, which do not have Li-Li in its nearby area [61]. The removed Li^+ are then inserted into anodic graphitic matrix, through a two-stage electrochemical process, which can be illustrated by the following two transformation reactions (Eqs. 1 and 2 respectively) [62, 63]. The first stage, which typically occurs at a voltage plateau of ~ 4 V, is attributed to the single phase reaction (Eq. 1) and while the second step (around 4.1 V) is associated to the two phase single reaction (Eq. 2) [64]. During discharge, a reverse similar process takes place and Li^+ are inserted back into spinel structure. This two-step process is well-explained through cyclic voltammetry. Each of those two pairs of peaks is attributed to one stage of the two-electrochemical charge–discharge processes of $LiMn_2O_4$ [60, 65] [60, 63].

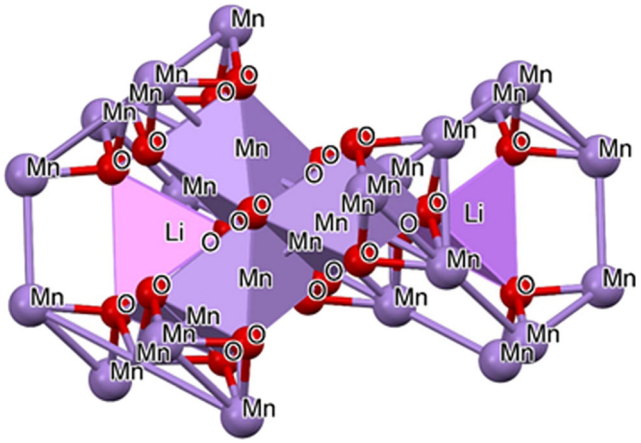

Fig. 2 Spinel structure of $LiMn_2O_4$ [54]

$$LiMn_2O_4 \rightarrow Li_{1-x}Mn_2O_4 + x0.5Li^+ + x0.5e^- \quad (x < 0.5) \tag{1}$$

$$Li_{1-x}Mn_2O_4 \rightarrow 2MnO_2 + (1-x)Li^+ + (1-x)0.5e^- \quad (x > 0.5) \tag{2}$$

The LMO's electrochemical behavior during cell's functioning is valid in both organic electrolyte solution (1 M $LiPF_6$ in EC:DMC (1/1 v/v)) and aqueous electrolyte solution (1 M Li_2SO_4) [66]. Li-ion batteries with organic electrolyte are efficient rechargeable batteries, with high operating potential, good average number of cycles, and high-energy density [67, 68]. However, high manufacture cost, need of expensive assembling installations, and flammable organic electrolytes determined a search for alternatives [67, 69]. J. R. Dahn et al. [70] suggested the replacement of the hazardous organic electrolytes with aqueous electrolytes. In this case, a cheaper lithium salt (e.g., $LiNO_3$, Li_2SO_4) is dissolved in water to obtain the electrolyte. Alias and Mohamad demonstrated, through an extensive study, the advantages of aqueous electrolyte solutions over organic electrolytes, by analyzing a series of indicators like cost assessment, safety concerns, electrolytes' ionic conductivity, and rate capability. Furthermore, characteristics of possible electrode materials for aqueous rechargeable lithium-ion batteries (ARLB) have been compared, taking in consideration aspects like crystal structure, morphologies, and

metal ions dissolution into the electrolyte, due to its large stability potential window in aqueous electrolytes (see Fig. 3). $LiMn_2O_4$ is regarded as an applicable cathode material for ARLB. Despite the advantages of aqueous electrolytes, there is still a long way until proper ARLB would be developed to satisfy the energy demand in practical applications [67].

In the following section of the current paper, the characteristics and parameters of the main synthesis methods for obtaining pristine $LiMn_2O_4$ have been discussed. Bare lithium manganese oxide can be manufactured through conventional methods like solid-state reactions (SSR) [71], sol-gel process (SGP) [3, 72], combustion method (CM), precipitation methods (PM) [11, 73], hydrothermal reactions (HR) [74–76], and spray-pyrolysis (SP) [77]. Also, new emerging synthesis methods like electrospinning [52, 78], template based syntheses [57, 79, 80], freeze-drying method [81], or polyalcohol assisted ion implanted method [82] have been briefly reviewed.

Synthesis method for pristine $LiMn_2O_4$

Solid-state reactions method is widely used as the main synthesis method for obtaining $LiMn_2O_4$, because it is a facile process and can be easily applied to industrial scale [83]. However, the main drawbacks, like poor crystallinity of the material, non-uniform particle size, and high-energy consumption, forced the researchers to look for other more efficient routes for the synthesis of $LiMn_2O_4$. Among the other investigated synthesis methods, sol-gel is intensive studied due to its advantages over the conventional solid-state method: samples of higher crystallinity, shorter heat treatment, and lower energy consumption. Sol-gel technique is not the only alternative synthesis method; other processes like combustion method, co-precipitation method, hydrothermal reactions, or spray-pyrolysis were successfully used to obtain high-performance LMO spinel.

A brief comparison between the main synthesis processes for obtaining $LiMn_2O_4$ is described in the Table 1.

SSR

In spite of the disadvantages mentioned above, solid-state reactions method is suited to be applied at industrial scale. Currently, SSR is used to obtain pristine $Li_xMn_2O_4$ powder, which is further improved by different novel protective coatings [89, 90].

The most common reagents for obtaining lithium manganese oxide by a solid-state process are manganese dioxide (MnO_2) and lithium hydroxide monohydrate ($LiOH{\cdot}H_2O$) or lithium carbonate (Li_2CO_3) [31, 91]. A possible chemical mechanism for SSR using MnO_2 and $LiOH{\cdot}H_2O$ as starting materials was described in details by Wang et al. [92].

The most important stages in a solid-state reactions process are the precursors mixing and the heat treatment. In a conventional synthesis, the precursors are ball-milled for a certain amount of time, usually, in the presence of ethanol [93] (Fig. 4). A comparative study on the ball milling effect upon the physical and electrochemical properties of $LiMn_2O_4$ was made by Wei et al. [84]. During the mixing operation, the precursors were milled for different time intervals (0, 2, 4, 6, and 8 h respectively). The best electrochemical characteristics were recorded for the sample milled for 6 h: 129.3 mAh g^{-1} (initial discharge capacity; 0.5 C) and a capacity loss of only 5.05% after 30 cycles. The spinel's stability has been tested by immersing the samples in electrolyte solution and measuring the Mn^{2+} concentration. It has been established that the lowest Mn ion (II) concentration was for the sample whose precursors were milled for 6 h.

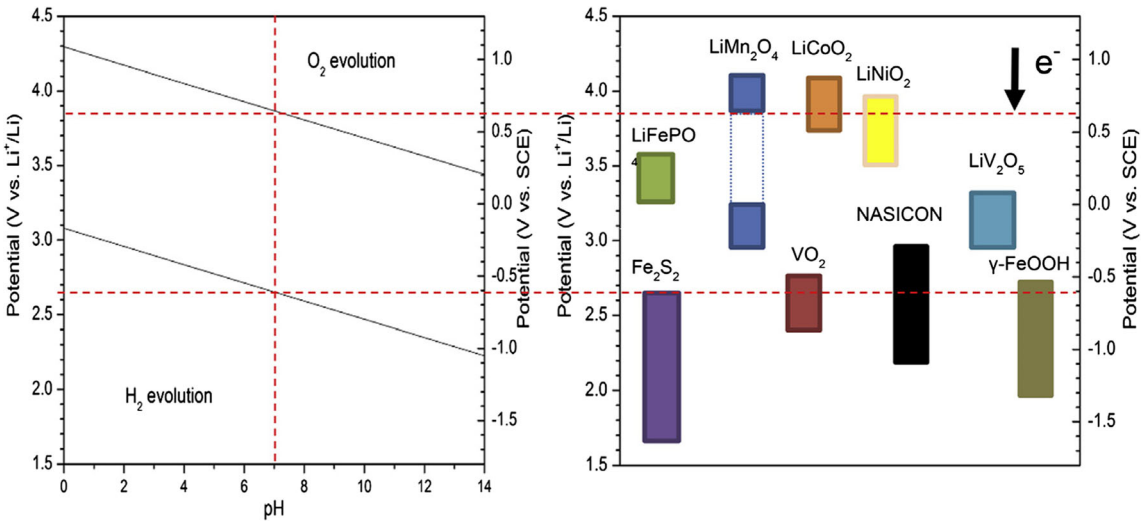

Fig. 3 Pourbaix diagram of lithium manganese oxide's stability in aqueous electrolyte [67] (reused with permission from Elsevier)

Table 1 A comparison of the main synthesis routes for obtaining $LiMn_2O_4$

Synthesis method	Advantages	Disadvantages
Solid-state reactions	-Simple process with few stages -Applicable at industrial scale	-Non-uniform particle distribution -Highly uncontrollable particle size -Possible non-uniform mixing of the reagents -High synthesis temperature -Long calcination period -High-energy consumption [19, 52, 84]
Sol-gel process	-Homogenous mixing of the reagents -Improved crystallinity -Relative shorter heat treatment -Lower synthesis temperature -Uniform particle distribution [20]	-Hard to be employed at industrial scale -Large quantities of precursors used in order to obtain the desired oxide amount -High amount of gaseous compounds -Expensive precursors
Combustion method	-High-surface area materials -Shorter heat treatment -Lack of additional calcination stages [48]	-Possible particles agglomeration [85]
(Co-)precipitation method	-High crystallinity of the synthesized material [83]	-Large particle distribution range [86]
Hydrothermal reactions	-Facile synthesis route -High reaction yield [86] -Lower synthesis temperature [87] -Lower energy consumption	-Expensive synthesis equipment [85]
Spray-pyrolysis	-High purity products -Short reaction time -Improved elimination of organic parts -Improved particle size control [77, 88]	-Low deposition rate -Waste of precursor solution [85]

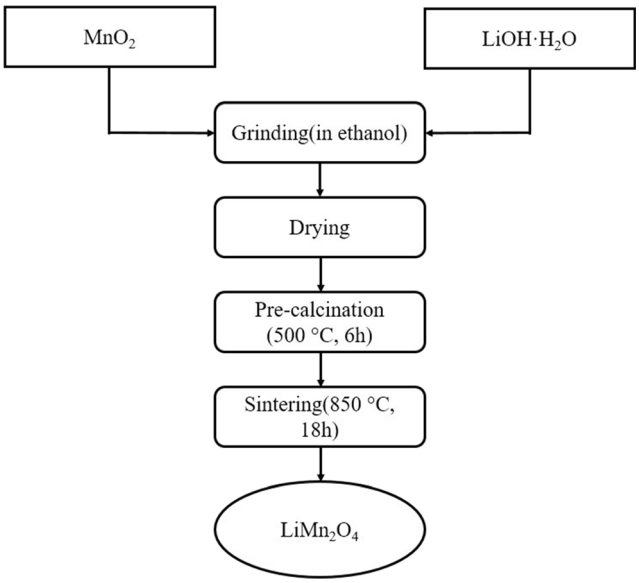

Fig. 4 Schematic representation of solid-state reactions method based of the data from ref. [93]

The morphologic characteristics of synthesized spinel have an important influence upon the electrochemical performance of the material. Over the years, scientists obtained, studied, and characterized different spinel's morphologies. One of the morphologies implied the formation of hollow spinel nanostructures [94–97]. Among the advantages of hollow morphology are smaller diffusion paths for lithium ions, improved host structure with better performances during charge/discharge cycles, and higher specific surface [94, 97].

Hollow LMO nanotubes for hybrid capacitors were synthesized through a SSR using $LiOH{\cdot}H_2O$ and as-prepared MnO_2-coated porous carbon nanofibers (PCNFs) [94] (Fig. 5). The MnO_2-coated carbon nanofibers were obtained through a two-stage synthesis, electrospinning and direct redox reaction. The time for the latter stage is crucial, because a short reaction time (10 min) leads to nanotubes fracture into nanoparticles, while a longer time (60 min) conducts to LMO formation along with Mn_3O_4 impurities, which hindered the spinel's performance during electrochemical tests. During the heat treatment, PCNFs ignition led to formation of LMO nanotubes, with

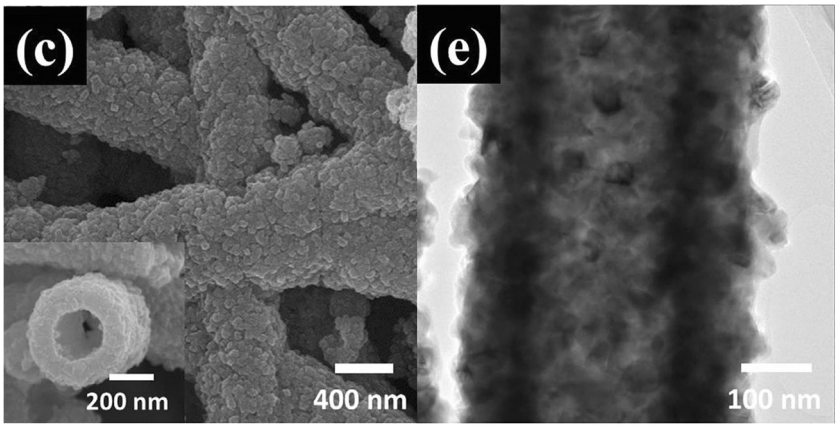

Fig. 5 **a** FESEM image and **b** TEM image of hollow LMO nanotubes obtained through SSR [94] (reused with permission from Elsevier)

holes' diameters between 210 and 231 nm and an average shell thickness of 136.85 nm. The initial discharge capacities for samples with the redox reaction time of 10, 30, and 60 min were 51.8, 73.5, and 60.1 mAh g^{-1}, respectively. The capacity for the samples with 30 min' redox reaction time is higher than the other samples due to shorter Li^+ diffusion paths characteristic to hollow nanotubes. All the synthesized samples delivered at least 90.0% of initial discharge capacities, after a number of 100 cycles (discharge rate of 1 C).

Mao et al. [95] synthesized LMO hollow microspheres (h-LMO) (see Fig. 6) with average diameters of 200–300 nm, by a modified solid-state reactions method. In order to compare the advantages of the modified SSR, pristine LMO (n-LMO) has been synthesized by conventional SSR process. N-LMO and h-LMO electrochemically tested, and it was noticed that the initial discharge capacity was higher for the latter (115.8 mAh g^{-1}). The first coulombic efficiency, for both samples, was below 90% due to possible side reactions and formation of the SEI layer. The hollow spheres not only presented a higher discharge capacity but also performed better when the electrode was cycled for 100 times (0.5 C), and only 16.8% capacity loss was recorded.

Kozawa et al. [96] studied the atmosphere influence upon the growth and morphology of LMO samples, using air and water-vapor atmosphere, respectively. LiOH-impregnated $MnCO_3$ spheres manufactured through a co-precipitation method were considered as precursors for $LiMn_2O_4$. High crystalline phases were obtained for the samples calcined between 600 and 800 °C. The temperature along with the calcination atmosphere played an important role for the obtained morphologies of the spinels. While compact large LMO particles were noticed for the sample calcined at 600 °C in water vapor, the LMO calcined at 800 °C and in atmosphere, exhibited hollow structures, which suggested that the particle development was mainly on the surface, while in the case of water vapor atmosphere, the particles grew both inside and on the surface.

Among the studied morphologies, there are the LMO nanorods. Using as-synthesized γ-MnOOH nanorods and $LiOH \cdot H_2O$ as precursors, Zhao et al. [98] synthesized $LiMn_2O_4$ nanorods through a facile and cost efficient SSR method (see Fig. 7). The manganese precursor (γ-MnOOH nanorods) was prepared by a HR, which implied the addition of anhydrous alcohol (CH_3CH_2OH). Low volume of alcohol, improved the $KMnO_4$ reduction to Mn^{2+}, which easily oxidized to Mn^{3+} because of oxygen presence, during the reaction time. As a result of solution alkalization through KOH releasing, the MnOOH was obtained in the solution and subsequent, via oxidation, γ-MnOOH nanorods formed. A higher amount of anhydrous alcohol provided a more powerful reduction media, which led to the obtaining of unstable γ-MnOOH and which soon became Mn_3O_4 (fact proven by XRD pattern). Several sintering temperatures in the range of 600–750 °C were studied. Well-shaped LMO nanorods were obtained at a temperature of 700 °C, and with the temperature increasing, the rod slightly shortened. The electrochemical tests of LMO showed the best cyclic performance for the nanorods sintered at 700 °C, with an initial discharge capacity of 128.7 mAh g^{-1} and a capacity retention of 89.5% after 30 cycles (1 C discharge rate). Electrochemical impedance spectra (EIS) were recorded for the sample calcined at 650, 700, and 750 °C, respectively; the lowest charge transfer

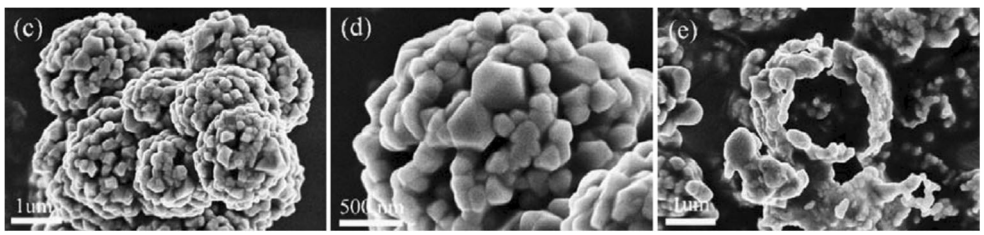

Fig. 6 **a**–**c** SEM images of hollow microspheres synthesized by Mao et al. [95] (reused with permission from Elsevier)

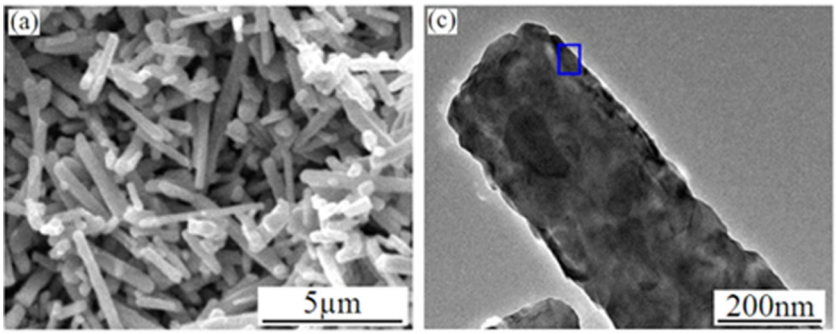

Fig. 7 **a** SEM and **b** TEM images of $LiMn_2O_4$ nanorods synthesized by solid-state reaction [98] (reused with permission from Elsevier)

resistance (R_{ct}) was calculated for the sample sintered at 700 °C (95.73 Ω) resulting in a lower charge–transfer resistance which facilitates good lithium ions diffusion.

LMO nanorods have been obtained by mixing (β-MnO_2 nanorods and $LiOH{\cdot}H_2O$) in pure ethanol, followed by a two stage heat treatment: pre-heating at 300 °C for 4 h and calcination at 750 °C for 24 h. The performance of LMO nanorods has been compared with the lithium manganese oxide synthesized employing MnO_2 precursors, without any specific morphology. LMO nanorods exhibited better electrochemical characteristics, by showing a discharge capacity of 119.6 mAh g^{-1} in the first cycle and retaining 86.2% of it after 100 cycles [99].

SSR is a high-energy consumptive synthesis method, which employs long and high-temperature calcination periods in order to obtain materials with improved electrochemical properties; thus, many research groups suggested different SSR methods, with one or two calcination stages, in inert or air atmosphere [100–102]. The heat treatment and main electrochemical parameters of the obtained LMO are indexed in Table 2. The most used manganese precursor is MnO_2, in different polymorphic state (α, β, and γ, respectively) [23, 102, 103]. As a lithium source, lithium carbonate [104] or lithium hydroxide [105] can be employed. Among the indexed synthesis procedures, there are several cases when the $LiMn_2O_4$ was tested in aqueous or hybrid aqueous electrolyte solutions which contained salts like $LiClO_4$ [106], $LiNO_3$ [107], Li_2SO_4 [100, 103], or a mixture of lithium and zinc acetates [108], respectively. In the other indexed cases, an electrolyte solution of $LiPF_6$ dissolved in a mixture of organic solvents (ethylene carbonate (EC) and dimethyl carbonate (DMC)) has been used.

Lithium manganese oxide obtained by simple solid-state reactions managed to deliver an average discharge capacity of about 120 mAh g^{-1} and managed to maintain at least 75% of the initial capacity after medium cycling tests (100 cycles). However, in several exceptional cases, extremely low or no capacity fading [23] has been calculated. Also, the LMO's morphology played an essential role in its amazing electrochemical performance at high discharge rates (4.5 C) in aqueous electrolyte, when the capacity retention was 88% after 1200 cycling.

Sol-gel process

Sol-gel is one of the most used synthesis techniques for obtaining high-purity, well-controlled stoichiometry, nanosized materials at relative low costs and temperatures, in comparison with high-energy consumption solid-state method [116–118].

In a typical sol-gel synthesis, acetates or nitrates of lithium and manganese are used as spinel's precursors, while citric acid is widely used as chelating agent [77, 119, 120] (Fig. 8). Ammonia solution is used during the precursor's homogenization in order to maintain a neutral pH.

In the last years, different modified sol-gel processes were developed, with the aim of improving the quality of $LiMn_2O_4$ cathode material.

Thirunakran et al. [3, 21, 22, 72, 122–127] investigated the influence of different novel chelating agents upon the formation and electrochemical performances of the pristine sample, maintaining the same heat treatment (see Table 3). The typical morphology observed for the synthesized spinel compounds was spherical uniform grains, with an average particles size of 0.5–1 μm [3, 122] (Fig. 9a). Involving lauric acid in the synthesis led to ice-cube particles with an average size of 200 nm (Fig. 9b), while myristic acid contributed to the formation of a cauliflower morphology, with nanometer-sized particles (~ 50 nm). A severe capacity loss (~ 30%) after just 1 cycles has been calculated for the LMO synthesized in the phthalic acid assisted sol-gel method. The powerful capacity loss is attributed to disordered and irregular spinel particles morphology. Lithium manganese oxide synthesized by a succinic acid modified sol-gel process exhibited the best performance, maintaining a high capacity of 136 mAh g^{-1} (99.2% of initial capacity), after 10 cycles at a c-rate of 0.5 C [128, 129].

Yi et al. [132] studied the temperature influence upon the material morphology, crystallinity, and electrochemical performance. It was found that a heat treatment of 800 °C for 10 h should provide good LMO crystallinity. The initial discharge capacity increased with the temperature raising, up to 130 mAh g^{-1} for the sample synthesized at 800 °C. No impurities were discovered for the sample calcined at 900 °C, but the spinel can suffer a disproportionate reaction by oxygen

Table 2 Solid-state reaction synthesis samples

No.	Precursors	Synthesis conditions		Particle characteristics		Tested electrochemical parameters						Ref
		Calcination parameters		Morphology	Particle size	Initial discharge capacity	Discharge rate	Cycling performance	Discharge rate	Testing temperature	Charge–transfer resistance (R_{ct})	
		Temperature (°C)	Duration (h)		(nm)	(mAh g^{-1})	(C*)	(mAh g^{-1} N^{-1})	(C)	(°C)	(Ω)	
1	Li_2CO_3 MnO_2	400 750	10 48	-By-pyramidal -Smooth and clean surface	300–400	109.7	1	78.4/100	1	RT	–	[100]
2		650 800	4 12			116	0.2	87 92.34	0.2	RT 60	–	[109]
3		350 800	12 24	-Agglomerated	< 200	113.5	0.2	80/50	0.2	RT	–	[107]
4		600 750	4 20	-Non-uniform -Smooth surface	800	122	1	88.7/100 66.3	1	RT 55	30.7	[110]
5		800	12	-Octahedral -Smooth facets	200	~ 100	0.5	40/100	0.5	55	32.8	[111]
6		350 750	10 10	-Agglomerated irregular	20,000	114.5	0.2	40/380	2	RT	–	[108]
7		600–650 750–800	8 10	-Regular-octahedral	1000	125.5	1	95.38/100 90.36/100	1	RT 60	144/100	[90]
8		600–650 750–800	8 10	Octahedral	1000	129.8 129.5	1	97.35/100 94.53/100	1	RT 60	193/100	[89]
9	Li_2CO_3	770	12	-Uniform	~ 200	120.4	0.2	87.53/20	0.2	RT	–	[112]
10	EMD	450 750	5 13	–	–	119.3 127.4	0.5	92.81/100 95.93/50	0.5	RT 55	97	[113]
11		750	24	-Uniform -Agglomerated	~ 800–900	124.4 123.29	0.2	105.8/40 96.5/40	0.2	RT 55	16.3/20	[63]
12		450 825	6 18	-Nonuniform	500–3000	128.1	0.5	62.1/100	0.5	RT	307.3/100	[1]
13	$LiOH·H_2O$ MnO_2	900	12	Octahedral	500	105 111.61	1	93.45/200 56/200	1	RT 60	–	[114]
14		320 750	12 8	-Microspheres	1000–8000	120.6	0.2	112.5/50	0.2	RT	–	[92]
15		700	5	-One-dimensional nanorod	150	118	0.1	94/30	0.1	RT	–	[115]
16		480	–	-Nanowires	8–9	125	0.1	105/100	60	RT	–	[102]
17		700	6	-Spherical	35	140	1	141/50	0.5		10	[23]
18		700	8	-Nanorods	80	105	9	103/1200	4,5		–	[103]
19		800	5	-Grains	100	120	1	62/100	1		–	[106]
20		750	10	-Uniform surface	100–300	129	0.2	103.2/380	2		–	[108]

RT room temperature

*1 C = 148 mAh g^{-1}

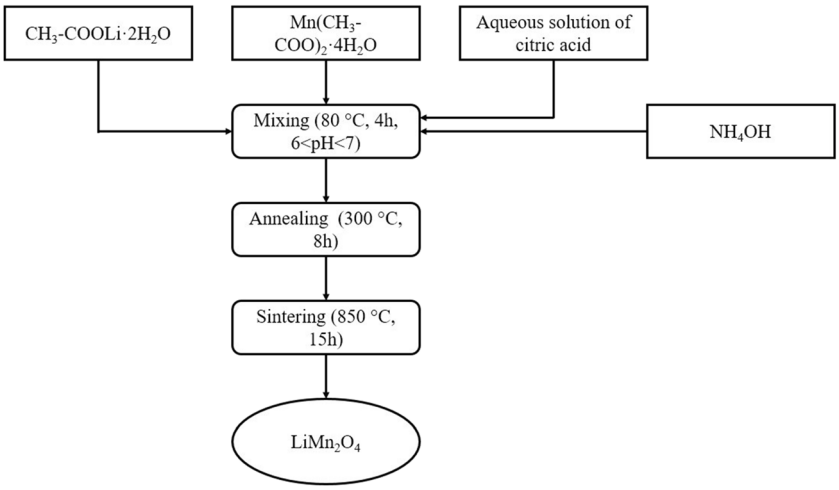

Fig. 8 Sol-gel process as indicated by the operations presented in ref. [121]

elimination, during cycling, resulting in two other phases, layered lithium manganese oxide ($LiMnO_2$) and discharged LMO ($Li_{1-2x}Mn_{2-y}O_{4-2x-y}$), which hinder the material's efficiency.

Hwang et al. [133] suggested an acrylic acid-aided sol-gel process and investigated temperature's influence upon the particle size, morphology, and electrochemical performances. Thus, the heat treatment ranged between 600 and 870 °C. Increasing the temperature size led to formation of spinels with higher crystallinity and larger average particle size. During electrochemical tests, it was observed that the material synthesized at temperatures above 800 °C suffered from severe initial discharge capacity and poor cycling life. These phenomena are related to higher content of Mn^{3+} ions, which are the main reason for the structural distortion and manganese dissolution into organic electrolyte. Any water trace, remained after battery's assembly, may react with $LiPF_6$, resulting into HF formation which damages the active cathode materials (like in the case of spinel, $Li_xMn_2O_4$, $0 < x < 1$), by destroying the solid electrolyte interface (SEI) and causing manganese dissolution into electrolyte solution. Manganese dissolution leads to capacity fade and shortened battery lifetime [63, 134, 135].

Unevenly LMO particles were obtained by Mohan et al. [136] via sol-gel, whereas tartaric acid ($C_4H_6O_6$) was the chelating agent. Jahn–Teller distortion influenced greatly the material's performance at elevated temperature (55 °C) and after 100 cycles, only 56% capacity retention (70 mAh g^{-1}) was measured.

Michalska et al. [137] synthesized $LiMn_2O_4$ nanopowders via sol-gel method using citric acid as main complexing agent and acetic acid as secondary one, followed by the gel's drying

Table 3 Electrochemical Characteristics of $LiMn_2O_4$ synthesized using different chelating agents (experimental conditions: 0.1 C, $N = 10$ cycles, potential interval = 3–4.5 V, 1 C = 148 mAh g^{-1})

No.	Material	Chelating agent	Discharge capacity (mAh g^{-1})	Coulombic efficiency (%)	Discharge capacity (after N cycles) (mAh g^{-1})	Capacity fading (%)	Ref.
1	$LiMn_2O_4$	$C_8H_6O_4$	135	93	94.5	30	[22]
2		$C_4H_4O_4$					[127]
3		$C_5H_9NO_4$	122	68	106.14	13	[126]
4		$C_{16}H_{32}O_2$	132	73	112.2	15	[125]
5		$C_{12}H_{24}O_2$	124	95	114.08	8	[3]
6		$CH_3(CH_2)_{15}COOH$	130	92	115.7	11	[21]
7		$CH_3(CH_2)_{24}COOH$					[123]
8		$C_{14}H_{28}O_2$					[72]
9		$C_{21}H_{43}COOH$			114.4	12	[122]
10		$C_4H_6O_4$*	137	96.5	136	0.8	[128, 129]
11		$C_6H_8O_7$*	133	98	123	7.5	[65]
12		$C_7H_7NO_2$	122	99	112	10	[130]
13		$C_3H_6O_3$*	140	–	106**	24	[131]

*c-rate = 0.5 C

**$N = 200$ cycles

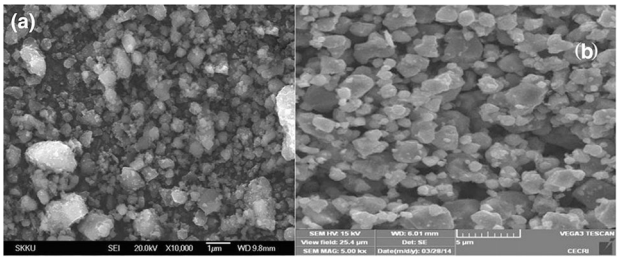

Fig. 9 **a** FESEM image of $LiMn_2O_4$ spherical grains synthesized by sol-gel method [122]. **b** SEM image of LMO cube morphology [3] (reused with permission from Elsevier)

at 150 °C for few hours and its calcination in a temperature range of 450–700 °C. Spherical shaped particle with good crystallinity and dimensions below 100 nm was obtained for the sample heated at 700 °C.

Low-temperature SGP was employed by Zheng et al. [138] to obtain bare LMO nanoparticles. Highly dispersed Mn_3O_4 and lithium hydroxide were used as manganese and lithium sources, respectively, while citric acid was the chelating agent. In order to promote the gelation, ethylene glycol was added during sol's stirring. The desired compound was obtained using a long low-temperature heat treatment, 550 °C for 15 h. The usage of manganese (II, III) oxide allowed the formation of pure spinel at low temperature. The electrochemical tests showed that LMO powder exhibited an initial discharge of 130 mAh g^{-1} and still managed to maintain 120 mAh g^{-1} (~ 96% capacity retention), after the cell was cycled for 200 cycles, 1 C and 25 °C. Even when the cell was cycled for 100 times at 55 °C, $LiMn_2O_4$ presented a capacity fade of only 14% (specific capacity of 111 mAh g^{-1}). Cycling the cell at small and high c-rate, respectively, the material proved good electrochemical reversibility, although, at 10 C, a loss of 52% from its initial capacity has been calculated.

Pristine lithium manganese oxide nanopowder has been synthesized by Michalska et al. [139] through a modified SGP, using two complexation agents. First chelating agent has been added during the solutions stirring, while either a polymerization agent (ethylene glycol) or the second chelating agent (acetic or glycolic acid) has been poured during solution's mixing. The resulted xerogel was the subject of a similar heat treatment with ref. [137]. Similar morphologies (nanograins) and particle size (100–200 nm) have been obtained for the samples prepared using citric acid and polymerization agent or second chelating agent.

Multiple chelating agents (citric and glycol) have been used in a SGP by Li et al. [140] . The working electrodes with embedded spinel cathode material were tested at elevated temperature (55 °C). The sample provided 79% of the theoretical capacity, while 34.4% capacity loss was recorded after 100 cycles, at a c-rate of 1 C. Similar to other papers, the spinel showed its limitations during the charge–discharge tests performed at 55 °C [141–143], but its performance was superior to ref. [144, 145], where same chelating agents, but different heat treatments, have been used. Higher sintering temperatures determine a raised risk for structural instability, which hinders the electrochemical performances of the compound.

Park et al. [69] obtained lithium manganese oxide throughout a sol-gel method, adding adipic acid in during solution's mixing. The obtained pristine LMO has been tested in 2 M Li_2SO_4 aqueous electrolyte in a novel symmetric geometry of laboratory Li-ion battery ($Li_xMn_2O_4$/electrolyte/$Li_xMn_2O_4$). Similar tests have been performed employing 1 M $LiPF_6$/EC:DMC (1:1 vol/vol) electrolyte; however, aqueous electrolyte solution proved enhanced rate capability with the increasing of current density, which can be attributed to the water's superior ionic conductivity (about two-magnitude order higher than organic solvents) [67, 69]. In aqueous solution, lithium manganese oxide provided a capacity of 110 mAh g^{-1}. Also, this novel design demonstrated the ability of LMO to be used both as anode and cathode.

Liu et al. [146] investigated a high voltage ARLB with TiO_2 nanotubes as anode, $LiMn_2O_4$ as cathode material and mixed lithium salt solutions as electrolyte. For the $LiMn_2O_4$ formation, a sol-gel based synthesis with hexanoic acid as chelating agent was realized. The spinel performance in aqueous mixed electrolyte solution was better than in organic electrolyte, hence providing a density of 134.9 mAh g^{-1} after 10 cycles, at c-rate of 10 C, and low capacity fade after 100 cycles (~ 9%) were recorded, respectively. The suggested ARLB cell with an operating voltage of more than 2 V (higher than the classical aqueous battery systems) can become an environmental friendly and low-cost power source for nowadays devices.

Wang et al. [147] created an innovative design for an ARLB's lithium-metal anode, which has been coated with homemade gel polymer electrolyte (sandwiched structure consisted of PVD/PMMA/PVDF and organic electrolyte) and LISICON film. An ARLB has been assembled using coated lithium metal as anode, $LiMn_2O_4$ as cathode and a solution of 0.5 M Li_2SO_4 as electrolyte. During voltammetry tests, the cell had an output voltage higher than 3.8 V, which is well above the water's theoretical decomposition voltage (1.23 V). By using the modified lithium-metal anode, the risk of lithium dendrites has been cut down. The main advantages of this design are related to longer cycle life, without the harmful action of HF resulted from $LiPF_6$, low environmental risk, cheap manufacture and high-energy density. The performance of the current ARLB was not hindered by the spinel's structural transition, even though Jahn–Teller distortion has been noticed.

$LiMn_2O_4$ with special nanochains morphology was obtained by Tang et al. [148] and demonstrated amazing performances, in a laboratory ARLB. When the cell was cycled at 91 C, 86% of the discharge capacity recorded for a lower c-rate (4.5 C) was still furnished (95 mAh g^{-1}). LMO

nanochains also proved its efficiency when the cell was cycled for 200 cycles (c-rate 4.5 C), and almost no capacity loss has been computed.

The sol-gel synthesizes, which employ citric acid as chelating agent, are indexed in Table 4. Among the best results, pristine lithium manganese oxide octahedral particles, synthesized by a citric acid aided sol-gel process [149] (Fig. 10, octahedral morphology), exhibited good discharge capacity in the first cycle (127 mAh g^{-1}) and a capacity fade of only 0.12 mAh g^{-1} per cycle.

Combustion method

Combustion method is regarded as an adequate synthesis process to obtain nanomaterials with high surface area and good crystallinity. One of the main advantages of combustion process is that there is no need for supplementary calcination stages, because of fuel usage (glycine, urea, citric acid) which auto ignites during the heating treatment and provides the necessary amount of heat to obtain the desired material structure [48, 161]. Combustion synthesis process can be applied either for solutions (solution combustion (SCS)) (Fig. 11) or for solid precursors [162].

Many studies focused on using urea as fuel in solution-combustion methods for synthesizing lithium manganese oxide (see Table 5). Lithium nitrate and hydrated manganese nitrated were mainly used as lithium and manganese precursor, respectively.

In most of the cases, a single annealing stage is enough to obtain LMO, but Nkosi et al. [163] suggested a different heat treatment approach. One part of the intermediate product obtained after xerogel's calcination at a lower temperature (550 °C) has been irradiated under microwave irradiation and the annealed at 700 °C, while another part has been subject of annealing followed by microwave irradiation. Involving microwave radiations prior to annealing stage boosted the electrochemical performances of nanograins LMO particles. Deploying an initial capacity of 131.5 mAh g^{-1}, lithium manganese oxide managed to provide 95% of its initial capacity after 50 cycles, at room temperature.

Glycine was also frequently employed as fuel in several combustion methods synthesizes. Şahan et al. [164–166] used glycine and nitrate precursors' solutions in a molar ratio of 1:4 in order to obtain pristine LMO spinels with average initial discharge rate of 115 mAh g^{-1}, when the cells were tested at 25 °C and ~ 110 mAh g^{-1} at elevated temperature (55 °C). $LiMn_2O_4$ exhibited relatively high capacity fading (25%) for electrochemical tests recorded at 25 °C. Poor capacity retention (around 50%) was noticed for all the samples cycled at 55 °C, due to Jahn–Teller distortion. All the samples synthesized through this method showed clear surface and uniform particle size distribution, in the range of 200–300 nm.

A comparative study between properties of samples obtained through a solution combustion method (SCS) with glycine as fuel and SSR was performed by Zhu et al. [170]. In both cases, identical calcination parameters (900 °C for 10 h) have been tested. Similar agglomerated morphologies have been noticed for both SCS and SSR samples, but SCS–LMO sample owned reduced particles size (500–1000 nm) (Fig. 12), ensuring superior electrochemical results. With an initial discharge capacity of 115.6 mAh g^{-1} and a capacity retention of 93%, after 50 cycles, overwhelmed the results measured for the SSR sample: only 80 mAh g^{-1} in the first cycle (which is not enough be applied for nowadays batteries) and a capacity retention of 90%. Even if single-phase LMO spinel characteristic XRD peaks were recorded for LMO obtained by SSR, the huge particle agglomeration hindered the material's performance during tests.

High-temperature ball milling aided combustion method has been employed to synthesize bare lithium manganese oxide [171]. The fuel used in that synthesis was citric acid. Milling temperature played an essential role for obtaining high crystalline sample, with small particle size and large surface area. It has been concluded that by adding citric acid and milling, the sample at 600 °C resulted LMO with high discharge capacity, 132 mAh g^{-1} (0.1 C), which lost only 5.3% of its capacity after 50 cycles.

The influence of different glycines: sucrose ratios on the morphology and electrochemical properties of spine have been investigated in ref. [172]. It was found that a percent of 98% glycine and 2% sucrose (G98-S2) enhanced better the spinel's capacity, in comparison with the samples obtained using other ratios (G95-S5, G90-S10, G80-S20). Primary particles have been relatively evenly distributed (100–200 nm in diameter) but have shown a tendency to agglomerate. Adding 2% sucrose determined the agglomeration reduction, from an average particle size of 6.228 μm (for the sample synthesized without sucrose) to 3.620 μm. In terms of electrochemical characteristics, G98-S2-LMO provided an initial discharge capacity (126.9 mAh g^{-1}), which was slightly higher than for the sample without sucrose.

Xu et al. [173] involved nitric acid in their solution combustion method, along with lithium nitrate and manganese acetate. No special fuel has been employed. No specific morphology has been obtained and the particles were rather agglomerated and irregular, with average size ranged between 120 and 430 nm. Limited lithium ions diffusion hindered $LiMn_2O_4$ performance and extremely low capacity was recorded at 5 C. However, when the c-rate was changed to 0.5 C, LMO recovered 92.3% of its initial delivered capacity.

(Co-)precipitation method

Precipitation and co-precipitation methods are relatively routes to obtain highly-crystalline spinels, with uniform

Table 4 Sol-gel method syntheses samples

No.	Precursors	Synthesis conditions		Particles characteristics		Tested electrochemical parameters							Ref
		Calcination parameters		Morphology	Particle size	Initial discharge capacity	Discharge rate	Cycling performance/number of cycles	Discharge rate	Testing temperature	R_{ct}	R_{SEI}	
		Temperature (°C)	Duration (h)		(nm)	(mAh g^{-1})	(C*)	(mAh g^{-1})/N^{-1}	(C)	(°C)	(Ω)	(Ω)	
1	LiAc	300	8	Spherical	150	135	0.5	81/100	0.5	30		98	[121, 150,
	MnAc	850 °C	15	shaped		125		62/100		60			151]
2		350	6	Cubic facets	~400	121	0.2	54.45/80	0.2	30			[152]
		800	12			118		33.04/80		55			
3		450	2	–	–	126.6	0.2	98.75/70	1	RT	141/=70	120	[153]
		800	16		–	125	1	68.75/70		60	–	–	
4		550	3	Spherical	20–30	–	–	–	–	–	–	–	[154]
5		300	0.08	Packed	~200	102.12	0.5	61.63/1000	0.5	25	–	–	[142]
		750	6			106.375		27.06/1000		55			
6		450	6	Grains	200–400	103	1			RT	–	–	[155]
		800	10			97.2	2	78.9/300	2				
7		300	3	Octahedral	150–200	127	0.8	114.93/100	0.8	RT	–	–	[149]
		750	12										
8		450	4	Polyhedral	100–300	110	1	72.05/50		RT	564	–	[156]
		850	7										
9		350	5	Irregular	100–500	82	1	84.18/200	1	25		8.35	[157]
		800	10			76.1		55.02/200		55			
10		450	5	Agglomerated	200–600	117.5	1	93.41/100	1	25	–	–	[62]
		750	10										
11		410	8–10		520–1240	47	0.5	32.2/40	0.5		–	400	[34]
		850	14										
12		300	24		30–50	111.4	1	88.1/100	1		35.8	19.7	[25, 158]
13	LiOH	450	8		200	134	0.5	108.54/30	0.5		132.4		[65]
	MnAC	750	18										
14	$LINO_3$	500	5	Uniform	100	122.5	0.3	113.2/40	0.3	RT	–	–	[159]
	MnAc	600	2										
15	$LiNO_3$	700	12	Compact		114	0.5	98.6/50	0.5		–	–	[160]
	$Mn(NO_3)_2$					103		72.72/200	2	60			
16		800	6	Cubic	–	–	–	–	–	–	–	–	[81]
17	Li_2CO_3	350	2–3	Octahedral		57.57		30.92/60			102.7	2.05	[66]
	MnAc	750	12										

RT room temperature

*1 C = 148 mAh g^{-1}

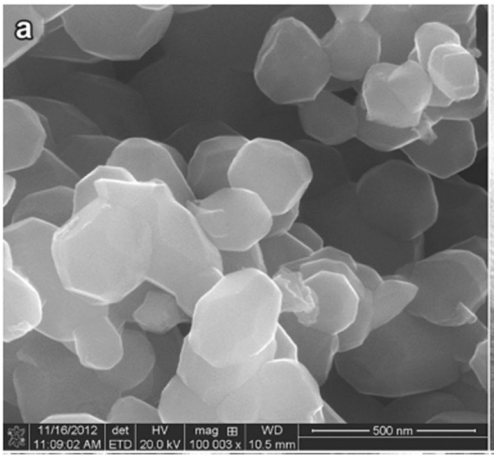

Fig. 10 Octahedral LMO particles obtained by sol-gel method [149] (reused with permission from Elsevier)

particle distribution. Moreover, (co-)precipitation methods exhibit advantages like short synthesis time, low energy consumption, and good yields [174]. In a precipitation process, the precursors for lithium and manganese salts are dissolved in water and by water evaporation, a precipitate is formed. The precipitate is subject for a heat treatment (Fig. 13).

Throughout a precipitation route, Zhu et al. [11] fabricated irregular shaped lithium manganese particles. The material was undergone to electrochemical tests in an ARLB. The initial discharge capacity (109.2 mAh g^{-1}) is comparable to the one achieved in organic electrolytes [156], and a quite low capacity fade (10.6%) was recorder after 50 cycles. When high c-rates were set (5 and 10 C, respectively), pristine LMO failed to prove good rate capability, delivering only ~ 82% of its capacity after 100 cycles.

Micrometer LMO spheres were synthesized by Yi et al. [175] by a mixed method employing two stages: facile co-precipitation route and a SSR. Firstly, $MnCO_3$ spherical particles were obtained, starting from a $MnSO_4 \cdot H_2O$ solution, Na_2CO_3 precipitant, and NH_4OH chelating agent. Secondly, manganese carbonate was preheated at 480 °C for 6 h, in air atmosphere. Finally, it was mixed with lithium carbonate and calcined at 750 °C, for 20 h, in air. The uniform micrometer LMO spheres performed well electrochemically, delivering 124.3 mAh g^{-1} in the 1st discharge cycle and maintained 89.9% of the initial discharge after 100 cycles, at 25 °C. In spite the fact that an initial slightly higher discharge capacity was noticed at 55 °C, a strong capacity fade (about 42%) was recorded after 100 cycles. The charge–transfer resistance was determined using electrochemical impedance spectroscopy, and it was found that micrometer LMO spheres exhibited lower charge transfer resistance (117.8 Ω) than 565 Ω. [156] and 132.4 Ω [65].

Microwave-assisted co-precipitation method led to $Li_xMn_2O_4$ ($x = 0$; 0.05) possible cathode material, but no further conclusive electrochemical measurements have been made by the authors [176]. One of the advantages of the proposed synthesis was the shorter heat treatment required for obtaining crystalline products.

Lu et al. [57] suggested a two steps template free synthesis, including a precipitation stage of the precursors and their calcination at 700 °C for 10 h, in air atmosphere, to obtain lithium manganese oxide with porous structure. Micrometer large porous structures, constructed of nanometer particles, with large radial channels (300–500 nm), which facilitates fast kinetics by enhancing lithium ion diffusion during electrochemical tests, were observed by scanning electron microscopy (SEM). The porous LMO performed well not only at low discharge c-rate (0.1 C), when an initial discharge capacity of 132.9 mAh g^{-1} was recorded, but also at high capacity (20 C), when it managed to provide 100 mAh g^{-1} in the first cycle and a capacity retention of 86% after 200 cycles. Lithium diffusion coefficient was in the range of 10^{-10} cm^2 s^{-1}, two magnitude orders higher than for

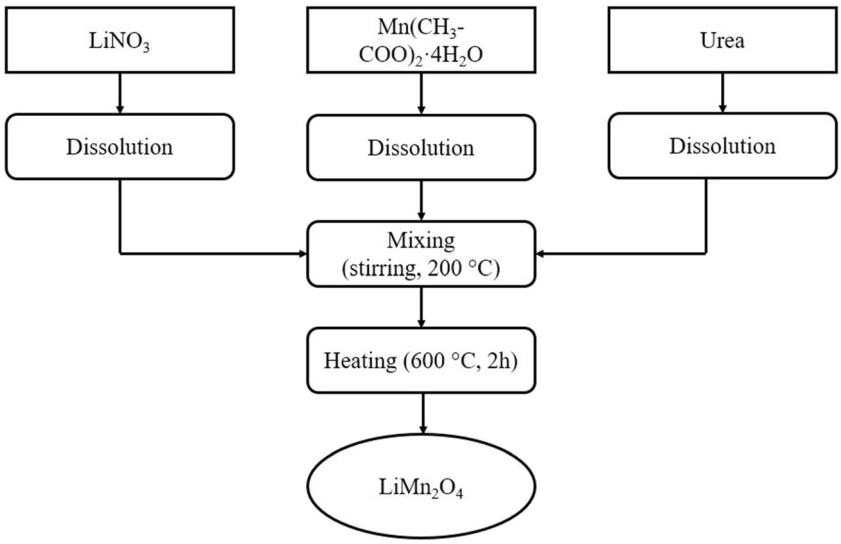

Fig. 11 Flow chart diagram for solution combustion method (SCS) as described in ref. [48]

Table 5 Specific parameters for $LiMn_2O_4$'s synthesis through combustion method using urea as fuel

No.	Synthesis conditions			Particles characteristics		Tested electrochemical parameters							Ref
	Precursors	Calcination parameters		Morphology	Particle size	Initial discharge capacity	Discharge rate	Cycling performance/ number of cycles	Discharge rate	Testing temperature	R_{ct}	R_{SEI}	
		Temperature (°C)	Duration (h)		(nm)	(mAh g^{-1})	(C*)	(mAh g^{-1})/N^{-1}	(C)	(°C)	(Ω)	(Ω)	
1	$LiNO_3$ $Mn(NO_3)_2{\cdot}4H_2O$	700	10	Spherical	1000–2000	122	0.1	73.2/50	0.1	RT	98.6	170.8	[167]
2				Cubic	500–1500	136	1	75/50	1		–	–	[120]
3		550 700	0.116 10	Grains	80–250	127.5	0.1	99.45/50	0.1				[163]
4		[a]				94.3		85.81/50					
		700	10										
5		700 [a]	10			131.5		124.93/50					
6		600	2	Nanorods	150	91	0.1	–	–	–	–	–	[48]
7	$LiNO_3$ $Li(CH_3COO){\cdot}2H_2O$ $Mn(NO_3)_2$	800	24	Agglomerated grains	200–500	121.3 123	1	100.8/200 93.5/100	1	25 55	62.05	–	[168]
8						118.2 118.6		96/300 83/200		25 55	75.6	–	[169]
9	$LiNO_3$ $Mn(NO_3)_2$	800	24	Agglomerated grains	100–400	121.3	1	107.95/80	1	RT	–	–	[49]

RT room temperature

*1 C = 148 mAh g^{-1}

[a] Distinctive heat treatment stage: Microwave irradiation at 600 W for 20 min

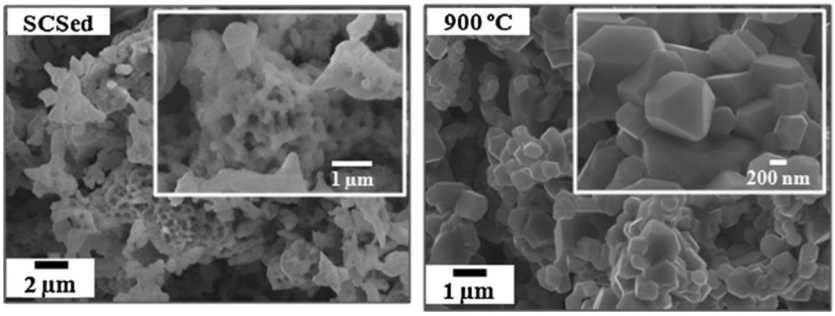

Fig. 12 Solution combustion porous precursor (left) LMO grains obtained through solution combustion method (right) [170] (reused with permission from Elsevier)

mesoporous LMO (1.7×10^{-12} cm^2 s^{-1}) [79]. Charge–transfer resistance value was extremely low (29.3 Ω) and, along with the other remarkable electrochemical characteristics, recommended this porous lithium manganese oxide for cathode material in Li-ion batteries (Fig. 14).

Hydrothermal reactions

Hydrothermal method (HM) is one of the most used synthesis routes to obtain advanced nanomaterials suitable for many technological fields, like ceramics, electronics, and biomedical. The main advantages, which recommend this synthesis route, are better nucleation control, low energy consumption, high purity compounds, and uniform particle distribution [177, 178]. One of the most employed HM is single-step hydrothermal reaction synthesis method (see Fig. 15).

The influence of aniline/$KMnO_4$ molar ratio and heat treatment upon the LMO formation through a HM has been investigated [179]. Hydrothermal synthesis took place at three different temperatures, 120, 150, and 180 °C, respectively. For the first temperature, it was demonstrated that the optimum ratio for obtaining pure spinel equals to 0.2:1, while in case of lower ratios (0.1:1; 0.15:1), $KMnO_4$ is reduced to birnessite and for a higher aniline content, and aniline reduced lithium manganese oxide to Mn_3O_4. Spinel's formation has been also facilitated by lithium hydroxide, not only birnessite. Pure LMO has been manufactured at the same molar ratio (0.15:1) at both 120 and 150 °C, but increasing the temperature to 180 °C, LMO was reduced to Mn_3O_4 starting with a molar ratio above 0.15:1. Normally, by increasing the temperature, the particle size increases, but in the present study, the particles obtained at 180 °C exhibited lower particle size (60–140 nm than the samples) (300–500 and 200–400 nm, respectively) synthesized at 120 and 150 °C, respectively. LMO-150 °C showed the highest initial discharge capacity (127.4 mAh g^{-1}), good cycling performance, and lowest charge–transfer resistance (187.1 Ω), which recommend the heat treatment of 150 °C.

One-step HM has been employed to obtain micrometer octahedral LMO particles by Ye et al. [180]. Starting from lithium acetate dehydrated, manganese acetate tetra hydrated, and potassium permanganate, the synthesis process is described by the following chemical reaction (Eq. 3):

$$5Li^+ + 7Mn^{2+} + 3MnO_4^- + 16OH^- \rightarrow 5LiMn_2O_4 + 8H_2O \quad (3)$$

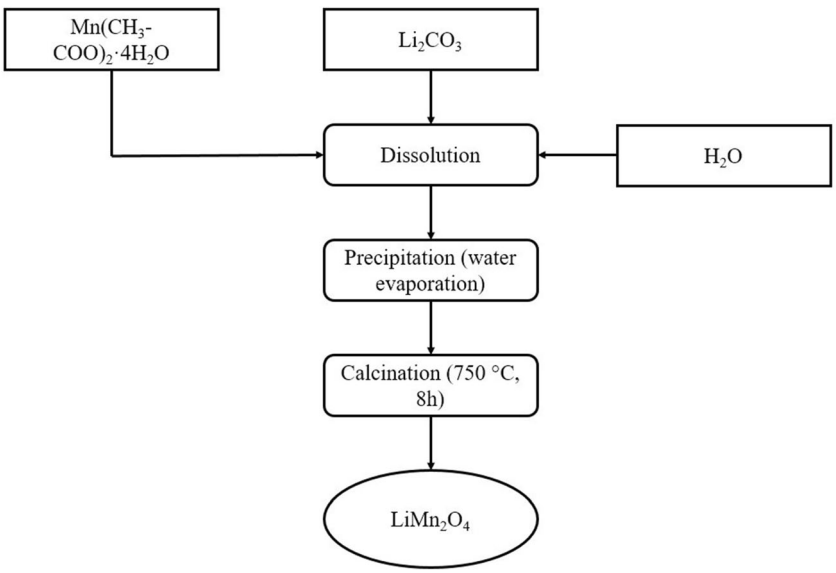

Fig. 13 Flow chart diagram for precipitation method based on data from ref. [83]

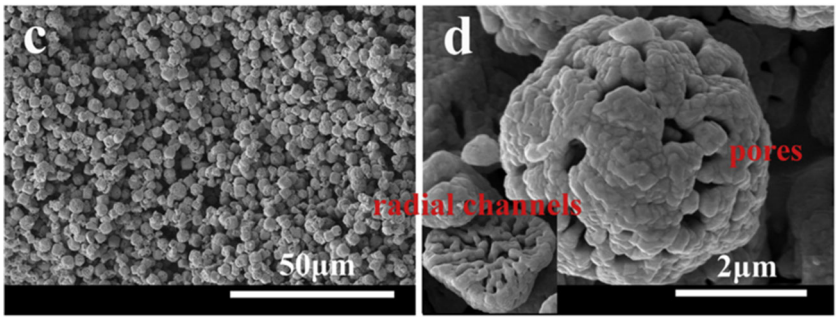

Fig. 14 SEM micrographs of porous $LiMn_2O_4$ structure as synthesized through precipitation method in ref. [57] (reused with permission from Elsevier); c) Overall SEM image of LMO particles, d) LMO macro-porous structure (close view)

The resulted $Li_xMn_{2-x}O_4$ ($x = 0.3$) delivered approximately 116 mAh g^{-1} in the fourth cycle (0.4 C). However, when the rate capability of the samples have been tested at different discharge currents, as-synthesized LMO samples failed to deliver more than 24 mAh g^{-1} at 20 C, while it showed a relatively decent discharge capacity at 5 C (84 mAh g^{-1}) or lower.

Normally, the hydrothermal reactions procedure temperature is at least 150 °C [75, 98, 180], but in ref. [101], a reaction temperature of 110 °C, for 12 h, led to formation of nanometer LMO particles. The as-synthesized particle was further heated to obtain nanoclusters. LMO clusters with a large BET area (65 m^2 g^{-1}), which delivered, in the first cycle, 81% of lithium manganese oxide theoretical capacity and preserved 84% after being cycle at 10 C. At higher c-rate (50 C), almost no capacity loss of LMO clusters has been recorded.

Homogenously dispersed lithium manganese microspheres (0.5–0.8 μm diameter) were obtained by a low-temperature (110 °C) and short time (8 h) hydrothermal synthesis [181]. LMO microspheres showed an initial discharge capacity of 127.9 mAh g^{-1} (0.1 C) and a coulombic efficiency of more than 99%. Also, its stability during repeated cycling was good and a capacity fade of only 5.4% was recorded after 60 cycles, demonstrating microspheres' stability.

A high-pressure hydrogen peroxide assisted HR method has been introduced by Sathiyaraj [182]. Precursors' mixture has been maintained in a pressured vessel at 140 °C, for 12 h. After the resulted precipitate has been dried and washed, no subsequent heat treatment has been needed. A possible reaction mechanism has been suggested (Eqs. 4–6):

$$Mn(NO_3)_2 + H_2O_2 \rightarrow Mn(OH)_2 + 2NO_2 + O_2\uparrow \quad (4)$$

$$Mn(OH)_2 + {}^1/_2H_2O_2 \rightarrow MnOOH + H_2O \quad (5)$$

$$MnOOH + LiOH + {}^1/_2H_2O_2 \rightarrow LiMn_2O_4 + 2H_2O \quad (6)$$

The obtained LMO nanorods, with 100 nm length and 50 nm in diameter, provided an initial discharge capacity of 118 mAh g^{-1}. A relatively high capacity fade (~ 9%) has been recorded in the first 10 cycles, but after that, the structure stabilized and in the following 40 cycles, only 2% of the initial capacity have been lost.

Crystalline lithium manganese oxide nanowires were synthesized by a HR method, followed by a two-stage calcination of the precursors' mixture [74]. NaOH and Mn_3O_4 were involved in the HR method to obtain precursor nanowires, which were further mixed with $LiNO_3$ and $LiCl{\cdot}H_2O$ and undergone a two-stage calcination treatment, at 500 and 800 °C for 3 h and 1 h, respectively. During the HR method, the optimal hydrothermal temperature for obtaining precursor nanowires, which maintained its morphology throughout calcination treatment, was 215 °C (for 4 days). The material was tested in an ARLB and similar initial discharge capacity (~ 110 mAh g^{-1}) was reported for LMO nanowires as in the case of LMO grains prepared by SSR [107]. The assembled ARLB ($LiV_3O_8/LiNO_3/LiMn_2O_4$ nanowires) furnished ~

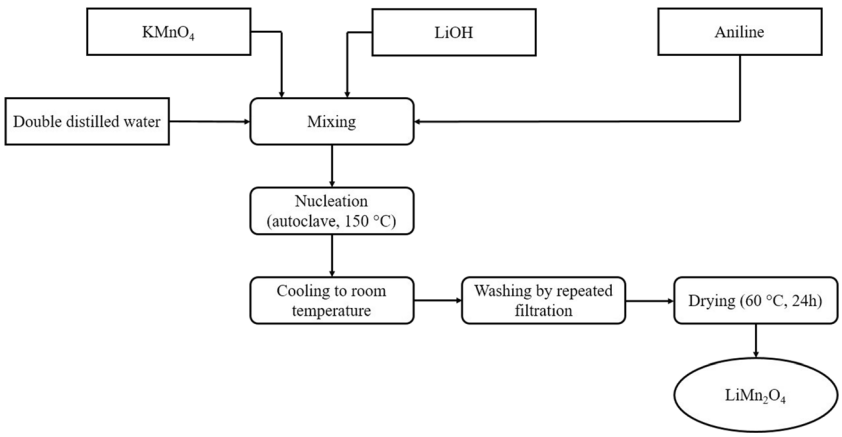

Fig. 15 Flow chart of one-step hydrothermal synthesis of $LiMn_2O_4$ based on experimental method described in ref. [179]

110 mAh g^{-1} in the first cycle and its capacity faded less at higher c-rates (10 C), demonstrating an increased stability over cycles. It has been suggested that longer time contact between electrode and electrolyte determined the poor performances at lower discharging rates (Fig. 16).

Other synthesis routes

An innovative synthesis route, based on controlling metal cations' hydration in organic solvent, has been to obtain ultrasmall LMO nanoparticles, based on controlling metal cations' hydration in organic solvent has been indicated by Miyamoto et al. [55]. Lithium manganese particles were synthesized by employing tetrabutylammonium permanganate ($TBAMnO_4$) as a precursor, which was dissolved in a 2-propanol-based LiCl solution and an extremely short heat treatment in moderate conditions (86 °C, 30 min). Very small particle size (2.3 nm), with large surface area (371 ± 15 m^2 g^{-1}) and short lithium diffusion paths, recommended the compound as a cathode material, but the crystallite was susceptible to agglomerate. Thus, graphene was used as agglomeration inhibitor and electronic conductivity promoter. During cell's cycling at a high discharge rate (100 C), an initial capacity of 134 mAh g^{-1} (90.5% of the theoretical capacity of 148 mAh g^{-1}) was delivered by the graphene modified lithium manganese oxide. Even though the material managed to exhibit 98.8 mAh g^{-1} after 10 cycles, the capacity fade (27%) was quite intense. An interesting fact about the ultrafine LMO particle was that it did not show the two plateaus (at 4.1 and 4.0 V), which are characteristic to spinel-type compounds.

Among other researched synthesis methods for obtaining LMO, one to be considered is spray drying process (Fig. 17). Spray drying method exhibits several advantages over SSR or sol-gel synthetic procedures: crystalline products, low cost, industrial scale applicability, and improved size and morphology control [88].

Dynamic sintering procedure during a two-step sintering spray-drying process led to perfect LMO microspheres [88, 105]. One single high-temperature (700 °C) sintering treatment could not provide spherical LMO particles, due to large eliminated quantities of gaseous compounds, mainly CO_2 (from acetates or carbonates involved in the spray drying process), which destroyed the spherical shape precursor particles. Static low sintering treatment (180 °C) did not have more successful, because the spherical shape could not be maintained, while the particles obtained in a rotating bed furnace, exhibited spherical shape, but particles surface shrinkage was noticed. Combining a low decomposition temperature along with a rotating movement assisted sintering treatment could provide perfectly shaped LMO spheres, because the gases were efficiently released and agglomeration was restrained. The precursors along with the heat treatment influenced the performance of the LMO spheres. For example, when manganese carbonate added to precursors' mixture, before spray-drying procedure [105] slightly boosted the initial discharge capacity (121 mAh g^{-1} at 0.2 C), while LMO obtained without $MnCO_3$ exhibited 117 mAh g^{-1} in the first cycle [88]. One possible explanation is that a more crystalline structure has been formed when the manganese carbonates was used, because an increased sintering temperature (800 °C) has been necessary to obtain lithium manganese oxide spinel structure; increasing the sintering temperature above 800 °C damaged spinel's structure. In both cases, with or without $MnCO_3$, similar capacity retention (95%) has been calculated after 50 cycles (Fig. 18).

In the last years, a series of polymers, like Pluronic P123 [79, 183], Pluronic F127 [184], and polyacrylonitrile [185], have been used in the recent developed polymer-aided template method (PATM). The synthesis parameters, along with the electrochemical performance of the obtained samples by PATM, are presented in Table 6. In the case of sample B, a mesoporous LMO structure, with large specific BET surface (42.5 m^2 g^{-1}), favored the lithium ions diffusion due to increased lithium diffusion paths and a discharge capacity of 133.6 mAh g^{-1} (90.2% of $LiMn_2O_4$'s specific capacity) has been achieved [79]. Mesoporous structure of sample C not only enhanced the low charge transfer resistance and large specific but also determined an improved lithium diffusion coefficient ($D_{Li} = 2.73 \cdot 10^{-12}$ cm^2 s^{-1}), much higher than for bulk LMO ($D_{Li} = 1.18 \times 10^{-12}$ cm^2 s^{-1}) [183]. Despite the fact that good cycling performances were noticed for sample C obtained at lower calcination temperature (500–600 °C), its significant reduced charge capacity (ranged between 76.3 and 96.5 mAh g^{-1}) does not recommend it as suitable electrode materials for practical Li-ion batteries. Heat treatment greatly influenced not only the spinel's formation but also particles' morphology [186] (Fig. 19).

By increasing the temperature from 600 to 700 °C and maintaining the same duration (6 h), the particles changed their shape from octahedron shape to (111) shape octahedral, while raising the calcination time (from 6 to 10 h),

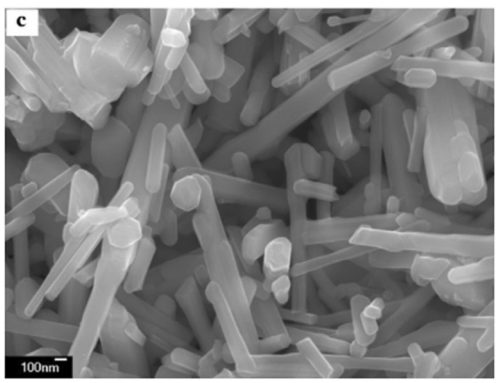

Fig. 16 LMO nanowires obtained by HR method [74] (reused with permission from Elsevier)

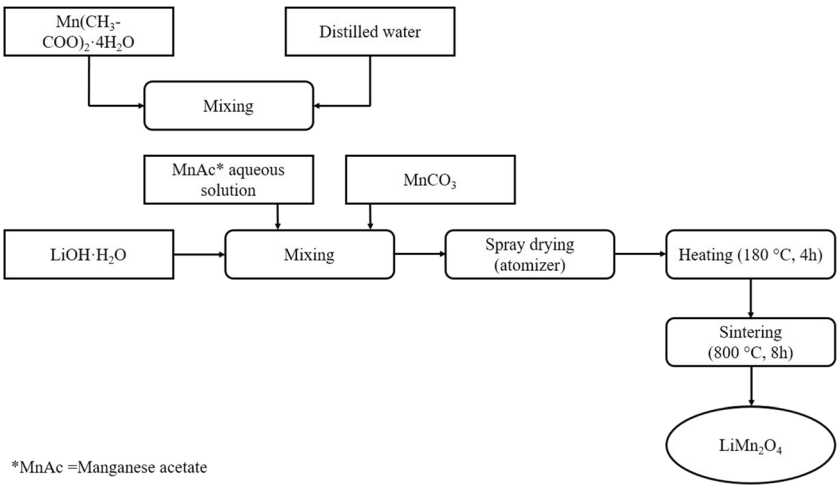

Fig. 17 Schematic representation of spray-drying process based on data inside ref. [105]

morphology has changed to truncated particles, with well-developed (111) planes and portions with (100) surfaces. Well-crystallized LMO truncated octahedral (sample D) calcined at 700 °C (10 h) succeeded to maintain a stable structure during cell cycling, and no capacity loss was recorded after 100 cycles.

Two-step template synthesis was employed by Chen et al. [80] in order to prepare hollow lithium manganese porous spheres. The first stage of the suggested method included the precipitation and calcination of $x\mathrm{MnCO_3}{\cdot}y\mathrm{CaCO_3}$ to obtain manganese dioxide, which was further calcined at 500 °C for 2 h to result Mn_2O_3 hollow microspheres. Before the second stage, different Ca^{2+}/Mn^{2+} ratios were investigated. The optimum ratio between calcium and manganese ions was 2:3, because in the case of lower ratio (1:3), dense MnO_2 formed, while at higher ratio (1:1), fracturable hollow MnO_2 structure was observed. The second stage was represented by a SSR method, when as-synthesized manganese oxide(III) was mixed with $LiOH{\cdot}H_2O$ and calcined at 800 °C for 12 h in air atmosphere to obtain the desired LMO product. Hollow LMO spheres (Fig. 20) presented a reasonable rate capacity by providing 104.2 mAh g^{-1} (88.3% of the initial discharge capacity of 117.9 mAh g^{-1}) after being cycled for 100 times at a c-rate of 1 C. The hollow porous spheres demonstrated a charge–transfer resistance in the 100th cycles (591.7 Ω) similar to R_{ct} value calculated for a polyhedral LMO sample in the first cycle (564 Ω) [156]. Also, the hollow structure proved its unique properties regarding lithium diffusion channels and a D_{Li} of 3.85×10^{-10} cm^2 s^{-1} was calculated, which is in good terms with the lithium diffusion coefficient calculated in other research (10^{-10} cm^2 s^{-1}) [57].

Qu et al. [188] developed a direct and facile template procedure to obtain porous LMO grains by involving polystyrene colloidal crystals as template. The synthesized material has been tested in an ARLB, which had an electrolyte solution of a 0.5 M Li_2SO_4. The porous LMO nanograins with a 3D structure yielded fast charging ability (76% of state of charge in only 40 min), low charge transfer, and amazing cycling ability (only 7% capacity fade, after 10,000 cycles at 9 C), which are superior to other $LiMn_2O_4$ functioning in an aqueous rechargeable lithium-ion battery [103, 155].

As-synthesized MnF_2 hollow polyhedrons served as template for obtaining Mn_2O_3 hollow polyhedron particles, which were used not only as anode material but also as precursor for $LiMn_2O_4$ hollow spheres [189]. LMO spinel was synthesized by employing a molten salt combustion method, in which the precursor salts were undergone a heat treatment of 800 °C for 10 h, in air atmosphere. The sodium chloride, which was added in a large quantity (three times more than the lithium and manganese precursors), promoted lithium ions diffusion

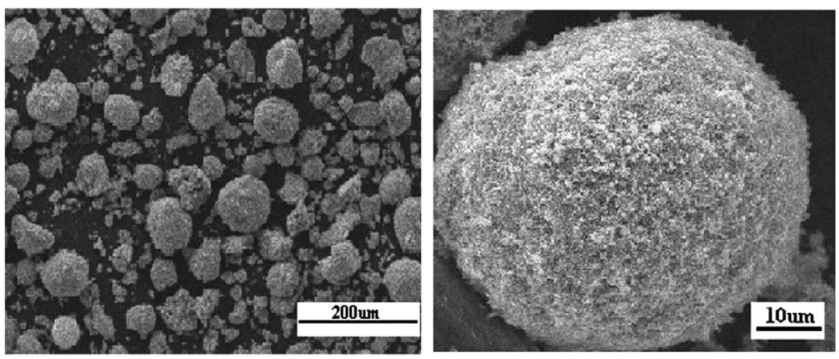

Fig. 18 Lithium manganese oxide microspheres as obtained in ref [105] (reused with permission from Elsevier)

Table 6 Pluronic P-123 and F-127 influence on LMO morphology and electrochemical performances

Samples	Copolymer	Heat treatment	Particle morphology	BET specific surface (m^2 g^{-1})	Initial discharge capacity (mAh g^{-1})	C-rate (C)	Capacity retention/number of cycles (%/N)	R_{ct} (Ω)	Ref.
A	P123	200 °C(1 h) + 600 °C (6 h)	Spherical crystal aggregates	1.18	76.3	0.1	99.9 / 10	106.3	[184]
B		750 °C (5 h)	Uniform sub-micron grains	42.5	133.6	0.5	81.7 / 100	*	[79]
C		300 °C (6 h) + 500 °C (6 h)	Uniform, regular shape particles	13.8	96.5	1	99.8 / 100	200.5	[183]
D		700 °C (10 h)	Truncated octahedral shaped particles	*	132.14		100 / 100	*	[186]
E		500 °C (3 h)	*	*	87		91 / 100	*	[187]
F		700 °C (12 h)	Homogenous compact particles	5.2	124	0.5	98.3 / 100	*	[160]
G	F127	200 °C(1 h) + 600 °C (6 h)	Ball-shaped agglomerated particles	0.70	84.8	0.1	99.9 / 7	124.6	[184]

*-Not mentioned in the article

to Mn_2O_3 surface and enhanced the reaction between precursors. Also, it favored the obtaining of uniform low-sized particles (100–200 nm), which formed LMO microspheres. Regarding electrochemical results, the LMO sample with NaCl as additive exhibited higher discharge capacity (117.5 mAh g^{-1}), better coulombic efficiency (84.7%), and improved cycling performance than the sample without NaCl.

The influence of graphite plates (800 and 15,000), with different specific area (4.24 m^2 g^{-1}(A) and 12.06 m^2 g^{-1} (B), respectively), over the morphology and electrochemical performances of LMO has been studied through a template synthesis [190]. Narrower B graphite plates failed to preserve its shape during the reaction and heat treatment and it started to split, while the larger thickness of A-graphite plates provided enough strength to retain its morphology. The conductive A-additive slightly increased LMO's discharge capacity (up to 124 mAh g^{-1}) and lithium diffusion coefficient (from 5.45×10^{-10} to 6.45×10^{-10} m^2 s^{-1}) and also diminished the capacity fade per cycle during cycle lifetime tests (30% capacity loss after 1000 cycles, 1 C). Another important aspect, which has a critical importance in LMO cyclability, is manganese dissolution in organic $LiPF_6$-based organic electrolyte. Lower BET area of graphite 800 mesh template favored the reduction of the manganese dissolution by half, in comparison with graphite 15,000 mesh.

Deng et al. [191] obtained porous core-shell $LiMn_2O_4$ microellipsoids via a facile template method, using hydrated lithium hydroxide and as-synthesized manganese carbonate ellipsoids as starting materials. The micrometer ellipsoid particles with average diameter of 1.5 μm and average length of 2.9 μm presented a BET surface area of 8.8 m^2 g^{-1} (Fig. 21), larger than spherical crystal aggregates [184], but much lower than other porous [52] and mesoporous [79] LMO spinels. Extended cycle lifetime at high c-rate has been demonstrated by core-shell $LiMn_2O_4$ microellipsoids and the capacity retention was 90% after 400 cycles, at room temperature. At elevated temperature, the initial discharge capacity of only 43.6 mAh g^{-1} increased to the maximum of 77.3 mAh g^{-1} and by the end of the test (200 cycles), it decreased to 59 mAh g^{-1} (23% capacity loss). The cycling performance of LMO at elevated temperature suffered from Jahn–Teller distortion and manganese dissolution. The porous structure determined low charge–transfer resistance (lower than 80 Ω), which had a positive action upon spinel's electrochemical performance, by shortening the lithium diffusion paths and enhancing faster kinetic of s Li^+ diffusion.

High-performance ultra-long LMO nanofibers have been obtained via a combined synthesis, involving electrospinning and sol-gel processes. In addition, the optimum ratio between PVP content, lithium and manganese precursors, and solvent was studied [192]. Uniform well-connected fibers were observed when the ratio PVP: LMO precursors: solvent = 6:6:88 (wt%). However, using another ration led to uneven distributed fragile fibers. The best electrochemical results

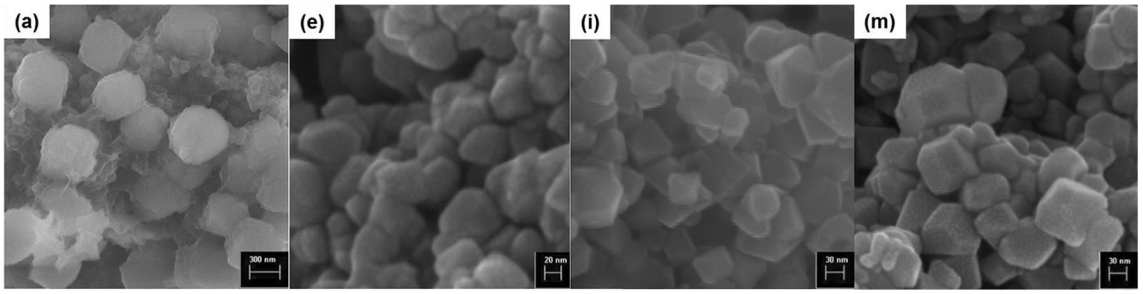

Fig. 19 **a** Irregular shaped LMO. **b** Octahedron LM. **c** Octahedral LMO. **d** Truncated octahedral LMO [186] (reused with permission from Elsevier)

were exhibited by long LMO fibers synthesized at a temperature of 700 °C for 8 h: initial discharge capacity of 128 mAh g^{-1} (0.5 C), 12% capacity fade, and high c-rate (30 C) discharge capacity (92 mAh g^{-1}). Due to structure stability, at low c-rate (0.1 C), LMO nanofibers exhibited a capacity (146 mAh g^{-1}) almost equal to spinel's theoretical capacity (148 mAh g^{-1}) and accomplished to recover 90% of the capacity after being cycled at 30 C.

Yang et al. [52] indicated that a low-temperature electrospinning technique to fabricate 1D hollow LMO nanostructure (Fig. 22) would overcome the disadvantages for obtaining commercial LMO: long heat treatment duration, high calcination temperature, and uneven particle size and morphology. The main advantages of the hollow 1D structures are related to large surface area, shorter lithium diffusion paths, and low deformation risk of spinel's primary unit cell during battery's cycling [52, 53]. Long ribbon-like hollow structures (500 nm), with an average wall thickness of 30–50 nm and large BET area (29.9 m^2 g^{-1}), were obtained at 500 °C. In comparison, in the same study, LMO was synthesized by a sol-gel method in the same conditions as for the electrospinning process and irregular particles with Mn_3O_4 impurities and lower BET surface were remarked.

Freeze-drying method provided good yield when it was studied as a possible LMO synthesis route. Precursor solutions were mixed and frozen at temperatures below −40 °C, while the pressure has decreased to several millibars. After the solvent (water) sublimated, the resulted precursor was heat-treated at least 600 °C [81, 193]. Partially sintered particles with an average diameter of 80 nm showed a good initial discharge capacity of 132 mAh g^{-1} (1 C) and it retained 73.25% of it after 300 cycles [193].

Recently, Li et al. [82] submitted a study which implied the synthesis of LMO particles by a polyalcohol assisted ion implanted method. This route consisted in mixing MnO_2 spheres with hydrated lithium hydroxide and an alcohol (ethylene glycol or glycerol), followed by LiOH dehydration, lithium ion implanting in MnO_2's pores and calcination at 800 °C for 6 h. It was observed that nanometer particles agglomerated into large porous micrometer spheres (~ 10 μm in diameter), which could assure adequate lithium ion diffusion paths. The rate capability of $LiMn_2O_4$ obtained by ion implanted method was very good, managing to recover 97.8% of its discharge capacity (123 mAh g^{-1}), when cell was cycled from 0.2 to 10 C and back to 0.2 C. Also, the material performed relatively similar during electrochemical cycle tests at 25 and 55 °C, respectively. In both cases, relatively low capacity losses (13% and 16%, respectively) have been calculated.

In a phase-inversion method, poly(methyl methacrylate) (PMMA) acted as a matrix and metal salts precursors were embedded into the matrix structure after the solvents have been removed by heating [194]. Later on, lithium manganese oxide was formed by precursor calcination at 700 °C, for 6 h. Relatively large uniform LMO spheres (~ 500 nm in diameter) were observed after heat treatment. A possible reason for the high BET surface (33 m^2 g^{-1}) and porous structure can be related to PMMA matrix removal during the calcination, causing the macropores (30–50 nm) occurrence. Galvanostatic tests showed a good discharge capacity of the material at high c-rates (5 C and 10 C), and the values are comparable to other studies, when LMO was synthesized by co-precipitation [11] and citric acid assisted sol-gel method [195].

Highly crystalline lithium manganese oxide thin films were obtained by manganese precursor electro-deposition on gold

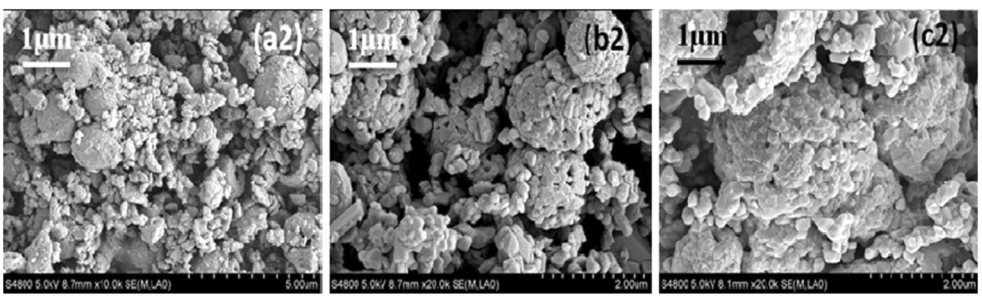

Fig. 20 Hollow LMO spheres obtained through a template method (LMO samples with the Ca^{2+}/Mn^{2+} ratio of 1:3, 2:3, and 1:1) [80] (reused with permission from Elsevier)

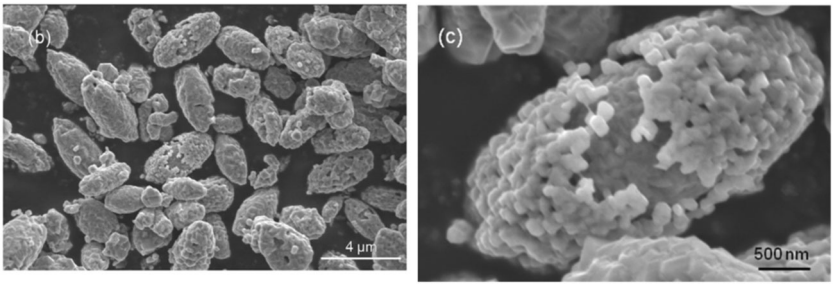

Fig. 21 FESEM micrographs. **a** $LiMn_2O_4$ microellipsoids. **b** Single porous LMO ellipsoid [191] (reused with permission from Elsevier)

substrate, followed by immersing in lithium hydroxide solution and calcination at 700 °C [119]. The charge flow rate is an important parameter, because long deposition times led to thicker films and, in one case (at higher charge flow rate, 50 mC), the particles from the film's surface began to agglomerate, resulting in lower lithium diffusion coefficient. The thinner films (deposited at 5 mC and 10 mC, respectively) performed very well, and almost no capacity loss has been calculated after a long cycling period (500 cycles). The lithium diffusion coefficients, calculated by Randles-Sevchik equation using cyclic voltammetry plots or estimated from EIS plots, were in the range of 10^{-9}–10^{-11} cm^2 s^{-1}, which are in good agreement with other similar results [57, 80, 180, 191].

Brief electrochemical characterization has been done by Zonghui Yi [196] in his study about lithium manganese oxide synthesized by a rheological phase reaction. The procedure, similar to hydrothermal reaction, implied the addition of deionized water, during starting materials' mixing, in order to form a rheological body. The obtained spinel material exhibited an initial discharge capacity of 111.2 mAh g^{-1} and a capacity loss of 21% has been recorded after 100 cycles (c-rate 0.2 C).

Pristine $LiMn_2O_4$ has been synthesized by a solution based route [197]. The salts were dissolved in ethanol and mixed together, followed by ethanol evaporation, precursor's pelletizing and calcination in oxygen flow at 900 °C for 12 h. The obtained hexahedral LMO particles exhibited an initial discharge of 115.2 mAh g^{-1} (0.2 C, 25 °C) and it faded with

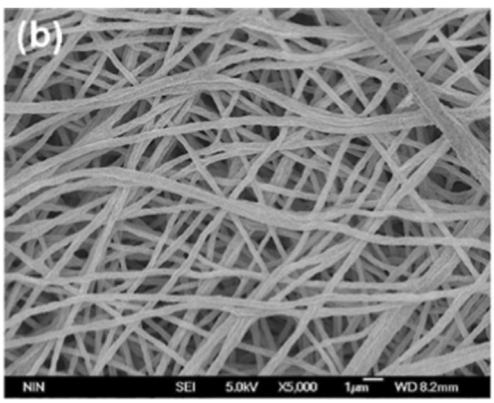

Fig. 22 1D hollow LMO nanorods obtained by low-temperature electrospinning technique [52] (reused with permission from Elsevier)

2.3 mAh g^{-1} per cycle, resulting a final discharge capacity of 103.5 mAh g^{-1} after 50 cycles. Manganese dissolution badly affected the elevated temperature performance of the LMO and only 79% of the initial capacity was delivered after 40 cycles. A deep ex situ XRD analysis has been made for investigating the unit cell transformation after a number of cycles. The analysis's conclusion confirmed that lattice cell parameter decreased in size after lithium ions extraction or intercalate, which has been attributed to greater concentration of Li^+ into Mn sites. A possible doping ion could stabilize the LMO structure.

Three-dimensional $LiMn_2O_4$ porous nanowalls (Fig. 23) were obtained by "hydrothermal lithiation" of deposited Mn_3O_4 precursor on Au or carbon cloth substrate [198]. As result of synthesis procedure, no conductive additive was needed when the working electrode was prepared. The optimum reaction's parameters for hydrothermal lithiation were 240 °C and 17 h. No different results were obtained in the case of a longer heat treatment (24 h). At lower temperature (200 °C), XRD pattern showed the presence of Mn_3O_4 impurities, while at 220 °C, even though there were no visible characteristic peaks for Mn_3O_4, the LMO peaks were not as sharp as at 240 °C. No distinctive morphologies were recorded, when different substrates were used, and the thickness of lithium manganese oxide interconnected nanowalls deposit on the substrate was between 20 and 50 nm. LMO nanowalls, with an initial discharge capacity of 131.8 mAh g^{-1}, performed exceptionally at room temperature and a capacity loss of only 4% was recorded after 200 cycles, 1 C. High c-rate performance is a key parameter for nowadays devices and the LMO deposited on Au/carbon cloth delivered an initial discharge capacity of 97 mAh g^{-1} at 20 C, similar to 1% wt. CeO_2-LMO [151], but higher than $LaMnO_3$-coated $LiMn_2O_4$ (68 mAh g^{-1}) [199].

Ammonium hydroxide has been used a chelating agent in a vacuum self-assembly reaction in order to obtain porous lithium manganese spinel with 3D framework [200]. Ammonia reacted with manganese acetate to form a complex ($Mn(NH_3)_n^{2+}$) and by ammonia's evaporation, the nucleation of $Mn(OH)_2$ occurred. Vacuum was used to suppress the oxidation of manganese hydroxide which has been obtained in the previous stage. The final synthesis step consisted in precursor's calcination at 700 °C for 8 h. Porous LMO showed

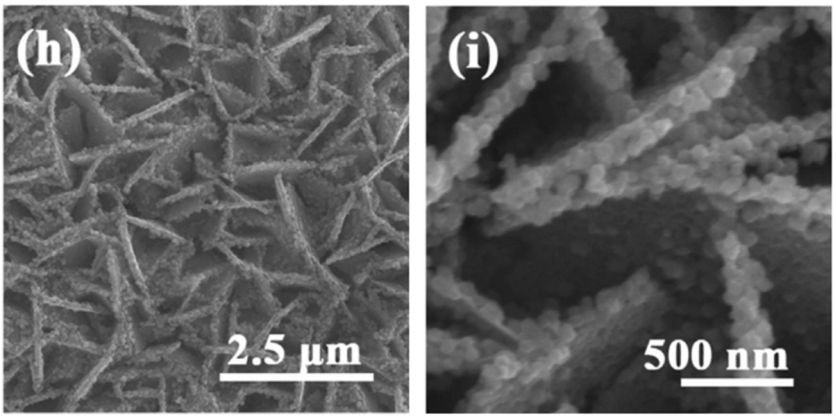

Fig. 23 FESEM images (h), i) different magnifications) of LMO porous nanowalls [198] (reused with permission from Elsevier)

remarkable results during all the electrochemical tests: high initial discharge capacity (131 mAh g^{-1}, 0.1 C), great capacity at high c-rates (96.9 and 92.6 mAh g^{-1} at 10 and 20 C, respectively) and good stability during charge–discharge cycles, because almost no capacity loss has been noticed after 100 cycles (95.9%, 10 C).

Conclusions

Lithium manganese oxide (LMO) is considered a suitable cathode material for emergent technologies, which implies the usage of adequate power sources. $LiMn_2O_4$'s advantages such as environmental friendliness, abundant raw materials, low production cost, and high rate capability recommend it as a cathode material for LIBs.

$LiMn_2O_4$ has two types of structure, layered [201] and spinel [46, 47], respectively, but only the spinel structured LMO is valuable for playing the cathode role in a Li-ion battery. However, hydrated layered LMO has been used for a facile synthesis of spinel type LMO [201]. In order to obtain LMO spinel, different synthesis strategies have been developed among them; solid-state reactions and sol-gel method are the most investigated, during the current review's studied timespan (2008–2019).

SSR can be easily used for large-scale industrial applications, because it does not imply complicated process stages. However, the high-energy consumption heat treatment and high risk of particles non-uniformness are the major drawbacks for SSR. It was noticed that the optimum sintering temperature for obtaining LMO ranged between 700 and 800 °C, when uniform particles with higher initial discharge capacity and good cycling ability were synthesized. One of the best results were observed for LMO spherical nanoparticles calcined at 700 °C [23], which almost delivered the theoretical capacity of the spinel (146 mAh g^{-1} vs 148 mAh g^{-1}) and maintained a capacity retention of 96.6% after 50 cycles at a low c-rate (0.5 C). Nanometric spherical LMO performed above average even in the case of increased discharge capacities, when capacities of 135, 127, and 98 mAh g^{-1} have been computed at 2, 5, and 10 C respectively.

Sol-gel technique provides oxidic materials uniform particle size, high crystallinity, and controllable stoichiometry. Alongside the reagents, chelating agents are needed in order to promote the formation of porous anhydrous structure with long interconnected polymeric chains. Nowadays, the most involved chelating agent in a sol-gel synthesis is citric acid. The chelating agent's role is very important and many scientists investigated the possibility of using one or more chelating agents or other chemical reagents, which can promote gel's polymerization. Materials with high discharge capacities were successfully obtained not only when citric acid has been employed [129, 150] but also in the case of succinic acid [128].

Hydrothermal reactions synthesis requires lower temperature than the SSR and SGP methods, but it needs special conditions, like high pressure. Normally, one synthesis stage is enough to manufacture products with good electrochemical properties. Such a good example are LMO nanoclusters with an initial discharge capacity of 120 mAh g^{-1}, which manifested great capacity retention even at extremely high discharge rate (50 C) [101]. Normally, the usual temperature for HR synthesis is around 160–180 °C [179]; it has been demonstrated that a lower temperature of 110 °C and a reaction time of minimum 8 h led to formation of performant spinels with increased cycling stability [181].

Single calcination stage and less energy consumption are needed in a combustion method, due to fuel's self-ignition during heat treatment. Combustion process can be applied for either solid or liquid precursors. The most used fuel is urea, but other fuels like glycine or citric acid have been studied.

Although many synthesis routes have been intensively studied and many others are just in the incipient phase, several key aspects like precursors' mixing time, heat treatment temperature, and duration still need to be carefully investigated for developing enhanced lithium manganese oxide spinels.

References

1. Zhao H, Liu S, Cai Y, Wang Z, Tan M, Liu X (2016) J Alloys Compd 671:304–311
2. Wang JG, Jin DD, Liu HY, Zhang CB, Zhou R, Shen C, Xie KY, Wei BQ (2016) Nano Energy 22:524–532
3. Thirunakaran R, Kim T, Yoon W-S (2016) Particuology 24:87–95
4. Ordoñez J, Gago EJ, Girard A (2016) Renew Sust Energ Rev 60: 195–205
5. Scrosati B (2000) Electrochim Acta 45:2461–2466
6. Pampal ES, Stojanovska E, Simon B, Kilic A (2015) J Power Sources 300:199–215
7. Xu X, Lee S, Jeong S, Kim Y, Cho J (2013) Mater Today 16:487–495
8. Mizushima K, Jones PC, Wiseman PJ, Goodenough JB (1980) Mater Res Bull 15:785–789
9. Zhang W-J (2011) J Power Sources 196:2962–2970
10. Mohan Rao M, Liebenow C, Jayalakshmi M, Wulff H, Guth U, Scholz F (2001) J Solid State Electrochem 5:348–354
11. Zhu Q, Zheng S, Lu X, Wan Y, Chen Q, Yang J, Zhang L-z, Lu Z (2016) J Alloys Compd 654:384–391
12. Li C, Zhang HP, Fu LJ, Liu H, Wu YP, Rahm E, Holze R, Wu HQ (2006) Electrochim Acta 51:3872–3883
13. Chen J-M, Cho Y-D, Hsiao C-L, Fey GT-K (2009) J Power Sources 189:279–287
14. Dai X, Zhou A, Xu J, Lu Y, Wang L, Fan C, Li J (2016) J Phys Chem C 120:422–430
15. Nayaka GP, Pai KV, Manjanna J, Keny SJ (2016) Waste Manag 51:234–238
16. Cho J, Jung H, Park Y, Kim G, Sup Lim H (2000) J Electrochem Soc 147:15–20
17. Nitta N, Wu F, Lee JT, Yushin G (2015) Mater Today 18:252–264
18. Li Z, Zhang D, Yang F (2009) J Mater Sci 44:2435–2443
19. Liu GY, Guo JM, Zhang LL, Wang BS, He Y (2012) Appl Mech Mater 142:205–208
20. Liu H, Wu YP, Rahm E, Holze R, Wu HQ (2004) J Solid State Electrochem 8:450–466
21. Thirunakaran R, Lew GH, Yoon W-S (2016) J Electroanal Chem 767:141–152
22. Thirunakaran R, Sivashanmugam A, Gopukumar S, Dunnill CW, Gregory DH (2008) Mater Res Bull 43:2119–2129
23. Kiani MA, Mousavi MF, Rahmanifar MS (2011) Int J Electrochem Sci 6:2581–2595
24. Waller GH, Brooke PD, Rainwater BH, Lai SY, Hu R, Ding Y, Alamgir FM, Sandhage KH, Liu ML (2016) J Power Sources 306: 162–170
25. Karaal Ş, Köse H, Aydin AO, Akbulut H (2015) Mater Sci Semicond Process 38:397–403
26. Liu J, Li G, Yu Y, Bai H, Shao M, Guo J, Su C, Liu X, Bai W (2017) J Alloys Compd 728:1315–1328
27. Ouyang CY, Shi SQ, Lei MS (2009) J Alloys Compd 474:370–374
28. Li X, Xu Y, Wang C (2009) J Alloys Compd 479:310–313
29. Wang X, Nakamura H, Yoshio M (2000) J Power Sources 110:19–26
30. Arumugam D, Paruthimal Kalaignan G (2008) J Electroanal Chem 624:197–204
31. Tao S, Zhao H, Wu C, Xie H, Cui P, Xiang T, Chen S, Zhang L, Fang Y, Wang Z, Chu W, Qian B, Song L (2017) Mater Chem Phys 199:203–208
32. Park K, Park J-H, Hong S-G, Yoon J, Park S, Kim J-H, Yoon D, Kim H, Son Y-H, Park J-H, Kwon S (2016) Electrochim Acta 222: 830–837
33. Shi T, Dong Y, Wang C-M, Tao F, Chen L (2015) J Power Sources 273:959–965
34. Ram P, Gören A, Ferdov S, Silva MM, Choudhary G, Singhal R, Costa CM, Sharma RK, Lanceros-Méndez S (2017) Solid State Ionics 300:18–25
35. Xuewu L, Xiaojuan W, Shuhua C, Jie T (2016) Mater Today Proc 3:672–680
36. Zhou D, Liu S, Wang H, Yan G (2013) J Power Sources 227:111–117
37. Chae C, Park H, Kim D, Kim J, Oh E-S, Lee JK (2013) J Power Sources 244:214–221
38. Zhao Y, Choe S-Y (2015) Electrochim Acta 164:97–107
39. Dai Y, Cai L, White RE (2012) J Electrochem Soc 160:A182–A190
40. Ando K, Matsuda T, Myojin M, Imamura D (2017) ECS Trans 75: 77–90
41. Wang J, Yu YY, Li B, Zhang P, Huang JX, Wang F, Zhao SY, Gan CL, Zhao JB (2016) ACS Appl. Mater Interfaces 8:20147–20156
42. Gotcu P, Seifert HJ (2016) Phys Chem Chem Phys 18:10550–10562
43. Bazuev GV, Tyutyunnik AP, Berger IF, Nikolaenko IV, Golovkin BG (2011) J Alloys Compd 509:6158–6162
44. Potapenko AV, Kirillov SA (2014) J Energy Chem 23:543–558
45. Thackeray MM, Picciotto LA, De Kock A, Johnson PJ, Nicholas VA, Adendorff KT (1987) J Power Sources 21:1–8
46. Thackeray MM, Johnson PJ, Picciotto LA, Bruce PG, Goodenough JB (1984) Mater Res Bull 19:179–187
47. Thackeray MM, David WIF, Bruce PG, Goodenough JB (1983) Mater Res Bull 18:461–472
48. Angelopoulou P, Paloukis F, Słowik G, Wójcik G, Avgouropoulos G (2017) Chem Eng J 311:191–202
49. Han C-G, Zhu C, Saito G, Akiyama T (2015) RSC Adv 5:73315–73322
50. Bensalah N, Dawood H (2016) J Mater Sci Eng 5:1000258
51. Julien C, Mauger A, Zaghib K, Groult H (2014) Inorganics 2:132–154
52. Yang G, Wang L, Wang J, Yan W (2016) Mater Lett 177:13–16
53. Yang G, Xu X, Yan W, Yang H, Ding S (2014) Electrochim Acta 137:462–469
54. Jain A, Ong* SP, Hautier G, Chen W, Richards WD, Dacek S, Cholia S, Gunter D, Skinner D, Ceder G, Persson KA (2013) APL Materials 1:011002
55. Miyamoto Y, Kuroda Y, Uematsu T, Oshikawa H, Shibata N, Ikuhara Y, Suzuki K, Hibino M, Yamaguchi K, Mizuno N (2015) Sci Rep 5:15011
56. Liu C, Neale ZG, Cao G (2016) Mater Today 19:109–123
57. Lu J, Zhou C, Liu Z, Lee KS, Lu L (2016) Electrochim Acta 212: 553–560
58. Ruffo R, Wessells C, Huggins RA, Cui Y (2009) Electrochem Commun 11:247–249
59. He P, Zhang X, Wang Y-G, Cheng L, Xia Y-Y (2008) J Electrochem Soc 155:A144
60. Bao S-J, Liang Y-Y, Li H-L (2005) Mater Lett 59:3761–3765
61. Xia Y, Yoshio M (1996) J Electrochem Soc 143:825–8233
62. Zeng J, Li M, Li X, Chen C, Xiong D, Dong L, Li D, Lushington A, Sun X (2014) Appl Surf Sci 317:884–891
63. Liu J, Wu X, Chen S, Liu J, He Z (2013) Bull Mater Sci 36:687–691
64. Sahan H (2008) Solid State Ionics 178:1837–1842
65. Zhao H, Liu X, Cheng C, Li Q, Zhang Z, Wu Y, Chen B, Xiong W (2015) J Power Sources 282:118–128
66. Cui Y, Yuan Z, Bao W, Zhuang Q, Sun Z (2012) J Appl Electrochem 42:883–891
67. Alias N, Mohamad AA (2015) J Power Sources 274:237–251
68. Scrosati B, Garche J (2010) J Power Sources 195:2419–2430
69. Park SI, Okada S, Yamaki JI (2011) J Novel Carbon Resource Sci 3:27–31
70. Li W, Dahn JR, Wainwright DS (1994) Science 264:1115–1118

71. Liu B-S, Wang Z-B, Zhang Y, Yu F-D, Xue Y, Ke K, Li F-F (2015) J Alloys Compd 622:902–907
72. Thirunakaran R, Lew GH, Yoon W-S (2016) WJNSE 06:1–19
73. Chan HW, Duh JG, Sheen SR (2003) J Power Sources 115:110–118
74. Zhao M, Song X, Wang F, Dai W, Lu X (2011) Electrochim Acta 56:5673–5678
75. Li X, Xiang R, Su T, Qian Y (2007) Mater Lett 61:3597–3600
76. Jiang CH, Dou SX, Liu HK, Ichihara M, Zhou HS (2007) J Power Sources 172:410–415
77. Ebin B, Lindbergh G, Gürmen S (2015) J Alloys Compd 620: 399–406
78. Li W, Zeng L, Wu Y, Yu Y (2016) Sci. China Mater 59:287–321
79. Chen S, Chen Z, Cao C (2016) Electrochim Acta 199:51–58
80. Chen P, Wu H, Huang S, Zhang Y (2016) Ceram Int 42:10498–10505
81. Seyedahmadian M, Houshyarazar S, Amirshaghaghi A (2013) Bull. Korean Chem. Soc. 34:622–628
82. Li W, Siqin G-W, Zhu Z, Qi L, Tian W-H (2017) Chin Chem Lett 28:1438–1446
83. Wang GG, Wang JM, Mao WQ, Shao HB, Zhang JQ, Cao CN (2004) J Solid State Electrochem 9:524–530
84. Wei C, Shen J, Zhang J, Zhang H, Zhu C (2014) RSC Adv 4: 44525–44528
85. Kopp Alves A, Bergmann CP, Berutti FA (2013) Novel synthesis and characterization of nanostructured materials. Springer, Berlin
86. Suvaci E, Adair HR (2001) In: Buschow KHJ, Cahn R, Flemings M, Ilschner B, Kramer E, Mahajan S, Veyssiere P (eds) Encyclopedia of materials science and technology, 2nd edn. New York, Elsevier
87. Shandilya M, Rai R, Singh J (2016) Adv Appl Ceram 115:354–376
88. Wan C, Wu M, Wu D (2010) Powder Technol 199:154–158
89. Feng X, Zhang J, Yin L (2016) Powder Technol 287:77–81
90. Feng X, Zhang J, Yin L (2016) Mater Res Bull 74:421–424
91. Ahn D, Song M (2000) J Electrochem Soc 147:874–879
92. Wang H-E, Qian D, Lu Z-g, Y-k L (2012) J Alloys Compd 517: 186–191
93. Li B, Wei X, Chang Z, Chen X, Yuan X-Z, Wang H (2014) Mater Lett 135:75–78
94. Sin D-Y, Koo B-R, Ahn H-J (2017) J Alloys Compd 696:290–294
95. Mao Y, Xiao S, Liu J (2017) Mater. Res. Bull 96(part 4):437–442
96. Kozawa T, Yanagisawa K, Murakami T, Naito M (2016) J Solid State Chem 243:241–246
97. Luo J, Cheng L, Xia Y (2007) Electrochem Commun 9:1404–1409
98. Zhao H, Li F, Liu X, Xiong W, Chen B, Shao H, Que D, Zhang Z, Wu Y (2015) Electrochim. Acta 166:124–133
99. Z-h C, K-l H, S-q L, Wang H-y (2010) Trans. Nonferrous met. Soc. China 20:2309–2313
100. Tron A, Park YD, Mun J (2016) J Power Sources 325:360–364
101. Lee S, Cho Y, Song HK, Lee KT, Cho J (2012) Angew Chem Int Ed Eng 51:8748–8752
102. Lee HW, Muralidharan P, Ruffo R, Mari CM, Cui Y, Kim do K (2010) Nano Lett 10:3852–3856
103. Tang W, Liu LL, Tian S, Li L, Li LL, Yue YB, Bai Y, Wu YP, Zhu K, Holze R (2011) Electrochem Commun 13:1159–1162
104. Jiang J, Du K, Cao Y, Peng Z, Hu G, Duan J (2013) J Alloys Compd 577:138–142
105. Wan C, Cheng M, Wu D (2011) Powder Technol 210:47–51
106. Sadeghi B, Sarraf-Mamoory R, Shahverdi HR (2012) J Nanomater 2012:1–7
107. Zhao M, Zheng Q, Wang F, Dai W, Song X (2011) Electrochim Acta 56:3781–3784
108. Yuan G, Bai J, Doan TNL, Chen P (2014) Mater Lett 137:311–314
109. Yang Z, Li S, Xia S-A, Jiang Y, Zhang W-X, Huang Y-H (2011) Electrochem. Solid-State Lett 14:A109
110. Chen Q, Wang Y, Zhang T, Yin W, Yang J, Wang X (2012) Electrochim. Acta 83:65–72
111. Lu J, Zhan C, Wu T, Wen J, Lei Y, Kropf AJ, Wu H, Miller DJ, Elam JW, Sun YK, Qiu X, Amine K (2014) Nat Commun 5:5693
112. Jiang QL, Du K, Cao YB, Peng ZD, Hu GR, Liu YX (2010) Chin Chem Lett 21:1382–1386
113. Sun H, Chen Y, Xu C, Zhu D, Huang L (2012) J Solid State Electrochem 16:1247–1254
114. Cho M-Y, Roh K-C, Park S-M, Lee J-W (2011) Mater Lett 65: 2011–2014
115. Nageswara Rao B, Padmaraj O, Narsimulu D, Venkateswarlu M, Satyanarayana N (2015) Ceram Int 41:14070–14077
116. Wu H, J-h L, Y-x C, Y-b S, Q-h Y (2002) J. Wuhan Univ. Technol. 17:21–24
117. Fu L, Liu H, Li C, Wu Y, Rahm E, Holze R, Wu H (2005) Prog Mater Sci 50:881–928
118. Yi T-F, Hu X-G, Dai C-S, Gao K (2007) JMater Sci 42:3825–3830
119. Quan Z, Ohguchi S, Kawase M, Tanimura H, Sonoyama N (2013) J Power Sources 244:375–381
120. Kebede MA, Phasha MJ, Kunjuzwa N, le Roux LJ, Mkhonto D, Ozoemena KI, Mathe MK (2014) Sustain. Energy Techn 5:44–49
121. Arumugam D, Paruthimal Kalaignan G (2010) Mater Res Bull 45: 1825–1831
122. Thirunakaran R, Lew GH, Yoon W-S (2017) J Energy Chem 26: 101–114
123. Thirunakaran R, Lew GH, Yoon W-S (2016) Powder Technol 301: 197–210
124. Thirunakaran R, Ravikumar R, Gopukumar S, Sivashanmugam A (2013) J Alloys Compd 556:266–273
125. Thirunakaran R (2014) J. Sol-Gel Sci. Technol. 69:397–406
126. Thirunakaran R, Ravikumar R, Vanitha S, Gopukumar S, Sivashanmugam A (2011) Electrochim. Acta 58:348–358
127. Thirunakaran R, Sivashanmugam A, Gopukumar S, Dunnill CW, Gregory DH (2008) J Phys Chem Solids 69:2082–2090
128. Arumugam D, Paruthimal Kalaignan G (2010) J Electroanal Chem 648:54–59
129. Arumugam D, Kalaignan GP, Vediappan K, Lee CW (2010) Electrochim. Acta 55:8439–8444
130. Thirunakaran R, Sivashanmugam A, Gopukumar S, Rajalakshmi R (2009) J Power Sources 187:565–574
131. Xiong LL, Xu YL, Tao T, Goodenough JB (2012) J Power Sources 199:214–219
132. Yi T-F, Hao C-L, Yue C-B, Zhu R-S, Shu J (2009) Synth Met 159: 1255–1260
133. Hwang J-T, Park S-B, Park C-K, Jang H (2011) Bull. Korean Chem. Soc. 32:3952–3958
134. Ren X, Wang J, Peng Z, Lu L (2018) Chem Sci 9:231–237
135. Xu G, Liu Z, Zhang C, Cui G, Chen L (2015) J Mater Chem A 3: 4092–4123
136. Mohan P, Paruthimal Kalaignan G (2014) Ceram Int 40:1415–1421
137. Michalska M, Lipińska L, Sikora A, Ziółkowska D, Korona KP, Andrzejczuk M (2015) J Alloys Compd 632:252–262
138. Zheng C-H, Wu Z-F, Li J-C, Liu X, Fang D-L (2014) Ceram Int 40:8455–8463
139. Michalska M, Lipińska L, Mirkowska M, Aksienionek M, Diduszko R, Wasiucionek M (2011) Solid State Ionics 188:160–164
140. Li X, Yang R, Cheng B, Hao Q, Xu H, Yang J, Qian Y (2012) Mater Lett 66:168–171
141. Yan J, Liu H, Wang Y, Zhao X, Mi Y, Xia B (2014) J Chem Eng Mater Sci 02:12–18
142. Lee JH, Kim KJ (2013) Electrochim. Acta 102:196–201

143. Kim W-K, Han D-W, Ryu W-H, Lim S-J, Kwon H-S (2012) Electrochim. Acta 71:17–21
144. Zhao S, Chang Q, Jiang K, Bai Y, Yang Y, Zhang W (2013) Solid State Ionics 253:1–7
145. Zhao S, Bai Y, Chang Q, Yang Y, Zhang W (2013) Electrochim. Acta 108:727–735
146. Liu S, Ye SH, Li CZ, Pan GL, Gao XP (2011) J Electrochem Soc 158:A1490
147. Wang XJ, Hou YY, Zhu YS, Wu YP, Holze R (2013) Sci Rep 3:5
148. Tang W, Tian S, Liu LL, Li L, Zhang HP, Yue YB, Bai Y, Wu YP, Zhu K (2011) Electrochem Commun 13:205–208
149. Aziz S, Zhao JQ, Cain C, Wang Y (2014) J Mater Sci Technol 30: 427–433
150. Arumugam D, Kalaignan GP (2011) Thin Solid Films 520:338–343
151. Arumugam D, Kalaignan GP (2010) Electrochim. Acta 55:8709–8716
152. Qing C, Bai Y, Yang J, Zhang W (2011) Electrochim. Acta 56: 6612–6618
153. Han SC, Singh SP, Hwang YH, Bae EG, Park BK, Sohn KS, Pyo M (2012) J Electrochem Soc 159:A1867–A1873
154. Rajesh YBRD, Dubey RS (2013) Nanoscience and Nanoengineering 1:139–141
155. Wang FX, Xiao SY, Shi Y, Liu LL, Zhu YS, Wu YP, Wang JZ, Holze R (2013) Electrochim. Acta 93:301–306
156. Guler MO, Akbulut A, Cetinkaya T, Uysal M, Akbulut H (2014) Int. J. Hydrogen Energy 39:21447–21460
157. Ming H, Yan Y, Ming J, Adkins J, Li X, Zhou Q, Zheng J (2014) Electrochim. Acta 120:390–397
158. Dombaycıoğlu Ş, Köse H, Aydın AO, Akbulut H (2016) Int. J. Hydrogen Energy 41:9893–9900
159. Jian-Kun T, Fu-Cheng W, Battaglia VS, Hai-Lang Z (2014) Int J Electrochem Sci 9:931–942
160. Yang Z, Jiang Y, Xu H-H, Huang Y-H (2013) Electrochim. Acta 106:63–68
161. Lee K-M, Choi H-J, Lee J-G (2001) J Mater Sci Lett 20:1309–1311
162. Zhou X, Chen M, Bai H, Su C, Feng L, Guo J (2014) Vacuum 99: 49–55
163. Nkosi FP, Jafta CJ, Kebede M, le Roux L, Mathe MK, Ozoemena KI (2015) RSC Adv 5:32256–32262
164. Şahan H, Göktepe H, Patat Ş, Ülgen A (2011) J Alloys Compd 509:4235–4241
165. Şahan H, Göktepe H, Patat Ş (2011) J Mater Sci Technol 27:415–420
166. Şahan H, Göktepe H, Patat Ş, Ülgen A (2010) Solid State Ionics 181:1437–1444
167. Kebede MA, Kunjuzwa N, Ozoemena K, Mathe M (2013) ECS Trans 50:1–14
168. Han C-G, Zhu C, Saito G, Akiyama T (2016) Electrochim. Acta 209:225–234
169. Han C-G, Zhu C, Saito G, Sheng N, Nomura T, Akiyama T (2017) Electrochim. Acta 224:71–79
170. Zhu C, Nobuta A, Saito G, Nakatsugawa I, Akiyama T (2014) Adv. Powder Technol 25:342–347
171. Li X, Shao Z, Liu K, Liu G, Xu B (2018) J Electroanal Chem 818: 204–209
172. Han C-G, Zhu C, Saito G, Akiyama T (2015) Adv. Powder Technol 26:665–671
173. Xu W, Li Q, Guo J, Bai H, C-w S, Ruan R, Peng J (2016) Ceram. Int. 42:5693–5698
174. Yang Z, Gredin P, Mortier M (2019) Opt Mater:109458
175. Yi X, Wang X, Ju B, Shu H, Wen W, Yu R, Wang D, Yang X (2014) Electrochim. Acta 134:143–149
176. Balaji S, Shanmugan S, Mutharasu D, Ramanathan K (2010) Mater. Sci. - Poland 28:583–593
177. Byrappa K, Adschiri T (2007) Prog. Cryst. Growth Charact. Mater. 53:117–166
178. Suchanek WL, Riman RE (2006) Adv Sci Technol 45:184–193
179. Lv X, Chen S, Chen C, Liu L, Liu F, Qiu G (2014) Solid State Sci 31:16–23
180. Ye SH, Bo JK, Li CZ, Cao JS, Sun QL, Wang YL (2010) Electrochim. Acta 55:2972–2977
181. Jiang Q, Wang X, Tang Z (2014) Fuller Nanotub Car N 23:676–679
182. Sathiyaraj K, Gangulibabu, Bhuvaneswari D, Kalaiselvi N, Peter AJ (2012) IEEE NANOTECHNOL 12:314–320
183. Hwang B-M, Kim S-J, Lee Y-W, Han B, Kim S-B, Kim W-S, Park K-W (2013) Int J Electrochem Sci 8:9449–9458
184. Hung IM, Yang Y-C, Su H-J, Zhang J (2015) Ceram Int 41:S779–S786
185. Koo BR, Ahn HJ (2017) J. Ceram. Process. Res 18:207–213
186. Hwang B-M, Kim S-J, Lee Y-W, Park H-C, Kim D-M, Park K-W (2015) Mater Chem Phys 158:138–143
187. Shi Y, Zhu S, Zhu C, Li Y, Chen Z, Zhang D (2015) Electrochim. Acta 154:17–23
188. Qu Q, Fu L, Zhan X, Samuelis D, Maier J, Li L, Tian S, Li Z, Wu Y (2011) Energy environ. Sci. 4:3985
189. He X, Wang J, Jia H, Kloepsch R, Liu H, Beltrop K, Li J (2015) J Power Sources 293:306–311
190. Tan XH, Liu HQ, Jiang Y, Liu GY, Guo YJ, Wang HF, Sun LF, Chu WG (2016) J Power Sources 328:345–354
191. Deng J, Pan J, Yao Q, Wang Z, Zhou H, Rao G (2015) J Power Sources 278:370–374
192. Zhou H, Ding X, Liu G, Jiang Y, Yin Z, Wang X (2015) Electrochim. Acta 152:274–279
193. Iturrondobeitia A, Goñi A, Palomares V, Gil de Muro I, Lezama L, Rojo T (2012) J Power Sources 216:482–488
194. Li Z, Yang J, Wang J, Tang J, Lei G, Xiao Q (2012) Microporous Mesoporous Mater 162:44–50
195. Michalska M, Hamankiewicz B, Ziółkowska D, Krajewski M, Lipińska L, Andrzejczuk M, Czerwiński A (2014) Electrochim. Acta 136:286–291
196. Yi Z (2016) J. Mater. Sci.: Mater. Electron. 27:10347–10352
197. Han D-W, Ryu W-H, Kim W-K, Eom J-Y, Kwon H-S (2013) J Phys Chem C 117:4913–4919
198. Xia H, Xia Q, Lin B, Zhu J, Seo JK, Meng YS (2016) Nano Energy 22:475–482
199. Wang C-M, Jin F-M, Shi T, Chen L (2016) J Electroanal Chem 775:306–310
200. Hua W-B, Wang S-N, Guo X-D, Chou S-L, Yin K, Zhong B-H, Dou S-X (2015) Electrochim. Acta 186:253–261
201. Jiang C, Tang Z, Zhang Z (2017) Ceram Int 43:11773–11779